

## DIPLOMARBEIT

# Experimental measurement of highly charged ion-induced electron emission from freestanding single-layer graphene

zur Erlangung des akademischen Grades

**Diplom-Ingenieur**

im Rahmen des Studiums

**Technische Physik**

eingereicht von

**David Weichselbaum**

Matrikelnummer 01629039

Ausgeführt am  
Institut für Angewandte Physik  
der Fakultät für Physik  
der Technischen Universität Wien

unter der Anleitung von  
Ass.Prof. Dr. Richard A. WILHELM  
Dipl.-Ing.<sup>in</sup> Anna NIGGAS  
und  
Univ.Prof. Dr. Friedrich AUMAYR

Wien, 15. Dezember 2021

---

David Weichselbaum

---

Friedrich Aumayr

---

Richard A. Wilhelm

## Abstract

The consequences of bombarding 2D materials with highly charged ions manifest in effects which include the ions capturing electrons and the emission of electrons from the material. The work described in this thesis is the commissioning and application of a hemispherical analyzer for the measurements of the energy distribution of emitted electrons at the NIELS experiment. The analyzer is checked for proper functionality during a test phase, where electrons emitted from tungsten wire are measured, which show that the analyzer works as intended. The test phase is conducted on a standalone test rig which is specifically designed and constructed for this purpose. Then, the hemispherical analyzer is mounted to the existing structure of the NIELS experiment. Heat cleaned single-layer graphene and gold samples are irradiated with  $\text{Xe}^{q+}$  ions ( $q \in [10, 30]$ ) whose energy range from 95 to 285 keV. For these measurements, a new target holder and a  $\mu$ -metal shield are designed and manufactured. The energy spectra of primary electrons emitted from single-layer graphene are measured via coincidence measurements, the ones of the gold sample without. Results show that the energy distribution of the emitted electrons are independent of both the charge state and the kinetic energy of the impinging ions, within the energy resolution of the used detector. However, single-layer graphene results indicate an increased electron yield with increasing incident ion charge state. In general, the majority of the emitted electrons possess energies below 10 eV, which supports the prediction of the model of Interatomic Coulombic Decay.

Furthermore, analysis of a time-dependent density functional theory simulation is conducted. The simulated scenario is the bombardment of single-layer graphene with one 100 keV  $\text{Xe}^{8+}$  ion. The goal of the analysis is to calculate the number of electrons captured by the ion and the number of electrons emitted from the graphene due to the interactions. The results predict that the Xe ion captures 6 electrons, while around 3 electrons are emitted from the graphene, which agrees with the calculation of the ion Hirshfeld charge. The simulation and its presented analysis thus pose a viable approach for calculating the number of captured and emitted electrons during ion irradiation.

## Zusammenfassung

Die Folgen des Beschusses von 2D-Materialien mit hochgeladenen Ionen äußern sich in Effekten wie dem Einfangen von Elektronen durch die Ionen und der Emission von Elektronen aus dem Material. In dieser Arbeit beschrieben ist die Inbetriebnahme und Anwendung eines halbkugelförmigen Analysators für die Messungen der Energieverteilung der emittierten Elektronen am NIELS-Experiment. Der Analysator wird in einer Testphase auf seine Funktionstüchtigkeit überprüft und es werden einige Messungen durchgeführt, die zeigen, dass der Analysator wie vorgesehen arbeitet. Die Testphase wird auf einem eigenständigen Prüfstand durchgeführt, der speziell für diesen Zweck entworfen und gebaut wurde. Anschließend wird der halbkugelförmige Analysator an die bestehende Struktur des NIELS-Experiments montiert. Hitzegereinigte einlagige Graphen- und Goldproben werden mit  $\text{Xe}^{q+}$ -Ionen ( $q \in [10, 30]$ ) bestrahlt, deren Energie zwischen 95 und 285 keV liegt. Für diese Messungen werden ein neuer Targethalter und eine  $\mu$ -Metallabschirmung entworfen und hergestellt. Die Energiespektren der von einlagigem Graphen emittierten Primärelektronen werden in Koinzidenz mit den Ionen gemessen, die der Goldprobe ohne. Die Ergebnisse zeigen, dass die Energieverteilung der emittierten Elektronen sowohl vom Ladungszustand als auch von der kinetischen Energie der auftreffenden Ionen unabhängig ist, innerhalb der Energieauflösung des verwendeten Detektors. Die Ergebnisse für einlagiges Graphen zeigen eine erhöhte Elektronenausbeute mit zunehmendem Ladungszustand der auftreffenden Ionen. Im Allgemeinen besitzt die Mehrheit der emittierten Elektronen Energien unter 10 eV, was die Vorhersage des Modells des interatomaren coulombischen Zerfalls unterstützt.

Des Weiteren wird eine Analyse einer zeitabhängigen Dichtefunktionaltheorie-Simulation durchgeführt. Das simulierte Szenario ist der Beschuss von einlagigem Graphen mit einem 100 keV  $\text{Xe}^{8+}$ -Ion. Ziel der Analyse ist es, die Anzahl der vom Ion eingefangenen Elektronen sowie die Anzahl der aufgrund der Wechselwirkungen aus dem Graphen emittierten Elektronen zu berechnen. Die Ergebnisse zeigen dass das Xe-Ion 6 Elektronen einfängt und etwa 3 Elektronen aus dem Graphen emittiert werden, was mit einer Berechnung der Hirshfeld-Ladung des Ions übereinstimmt. Die Simulation und die durchgeführte Analyse stellen somit einen brauchbaren Ansatz für die Berechnung der Anzahl der eingefangenen und emittierten Elektronen während der Ionenbestrahlung dar.

# Contents

<b>1</b>	<b>Introduction</b>	<b>1</b>
1.1	Outline . . . . .	1
1.2	Ion-solid interactions . . . . .	2
1.3	2D materials and motivation . . . . .	4
<b>2</b>	<b>Experimental Methods</b>	<b>7</b>
2.1	Hemispherical analyzer . . . . .	7
2.1.1	General description . . . . .	7
2.1.2	SPECS EA10+ . . . . .	9
2.2	Test rig . . . . .	15
2.2.1	Experimental setup . . . . .	15
2.2.2	Data acquisition . . . . .	16
2.3	NIELS . . . . .	19
2.3.1	General description . . . . .	19
2.3.2	Experimental setup . . . . .	20
2.3.3	Data acquisition . . . . .	21
<b>3</b>	<b>Results and Discussion</b>	<b>25</b>
3.1	Test phase . . . . .	25
3.2	Au (111) . . . . .	28
3.3	Single-layer graphene . . . . .	30
3.4	Discussion . . . . .	36
<b>4</b>	<b>TDDFT simulation</b>	<b>38</b>
4.1	General description . . . . .	38
4.2	Results . . . . .	39
<b>5</b>	<b>Summary and outlook</b>	<b>45</b>
	<b>Danksagung</b>	<b>47</b>
	<b>References</b>	<b>48</b>
<b>A</b>	<b>SolidWorks drawings</b>	<b>52</b>

# 1 Introduction

## 1.1 Outline

The effects of highly charged ions on materials are an intensively researched topic in the area of ion-solid interactions [1,2]. They play an important role in a wide range of applications, for example the modification of materials on the nano-scale [3]. For these modifications, highly charged ions can be used, as their potential energy plays an important role in the energy deposition [4–6]. Recently, ion-solid interaction research focussed on investigating 2D materials like the semi-metal graphene or the transition metal dichalcogenide monolayer molybdenum disulfide ( $\text{MoS}_2$ ) [7,8]. Measuring the properties of the ions after passing through such materials reveals charge-, energy-, and angle-dependent data, like the energy loss of the ions and their exit charge state [9–11]. An example are the angular and the charge state dependence of the energy loss of slow highly charged Xe ions in 1 nm thick carbon nanomembranes [12]. Moreover, experiments on freestanding graphene yielded that the charge exchange only weakly depends on the scattering angle, while the energy loss shows a significant dependence [13]. The cleanliness of the samples also influences those ion properties, which in turn offers a new way of evaluating the contamination of a sample using ion beam spectroscopy [14].

The ion-irradiated 2D materials also undergo changes, enabling defect engineering or the creation of specific nanostructures [15–18]. For example, theoretical research suggests that transition metal dichalcogenide/graphene heterostructures (e.g.  $\text{MoS}_2$ /graphene) with certain ion-induced defects are possible water electrolysis catalysts for hydrogen production and perform as well as platinum [19].

Another important aspect of ion-beam experiments are the electrons which are emitted from the sample during the interaction, i.e. ion-induced electron emission [20–22]. Such experiments offer insight into the electronic dynamics of the investigated materials and help understand the underlying processes behind ion-solid interactions.

The goal of the work described in this thesis was to put a hemispherical analyzer (HEA) into operation and to demonstrate its functionality through experimental measurements of ion-induced electron emission from single-layer graphene (SLG) and gold. Section 1.2 starts by explaining the various phenomena occurring during ion-solid interactions and how electrons are emitted throughout these processes. It is described how these phenomena change for 2D materials and provides a motivation for this thesis. The experimental methods are described in Section 2, starting with the basics of HEAs and the details of the specific analyzer which was used for the conducted measurements in Subsection 2.1. Subsection 2.2 outlines the test rig setup which was built for preliminary tests of the HEA as well as the used digital measurement setup. The setup of the NIELS experiment, where the main measurements took place, is described in Subsection 2.3, including the new data acquisition setup which was created specifically for coincidence measurements. Section 3 starts by discussing the results of the test measurements conducted with a tungsten wire as electron source (3.1). Furthermore, the energy distribution of electrons emitted from ion-irradiated gold are presented (3.2). Subsection 3.3 contains the SLG electron spectra which were measured in coincidence with the projectile ions. Lastly, they are discussed in Subsection 3.4. Besides the experimental part, additional work was carried out in order to calculate the captured and emitted electrons from the

results of time-dependent density functional theory simulations. The simulations, their analysis, and the results are presented in Section 4. A conclusion on the work is drawn in Section 5 by giving an overview of the conducted work and its results.

## 1.2 Ion-solid interactions

The field of ion-solid interaction is concerned with the effects which occur when ions approach the surface of materials and collide with it. These effects include the emission of electrons, photons, and atoms of the material (sputtering). Both electron emission and sputtering are subdivided further into a *kinetic* and a *potential* part. Kinetic contributions are defined by the kinetic energy of the ion, and it occurs through elastic, binary collisions with the target atoms or electrons. The potential part is defined by the charge state of the ion and leads to both potential electron emission and sputtering ([23]), which are mostly independent from the kinetic part. Depending on the involved atom species, the projectile ions themselves are either scattered off the sample or they are implanted. During these interactions they modify the structure of the solid, for example by creating nano-structures or interstitial defects.

When a positively charged ion comes close to the surface of a solid, the ion captures valence electrons of the material through resonant electron transfers. One theoretical model describing these transfers is the classical over-the-barrier model [24]. If the ion is in a high charge state, highly excited Rydberg states of the ion are occupied through such electron transfers. Lower states stay unoccupied, resulting in a so-called *hollow atom* [25]. The highly excited electron states of the hollow atom then quickly decay through various processes. A schematic of atomic de-excitation and neutralization mechanisms is shown in Figure 1.

**Resonant electronic transitions** or resonant electron transfers are non-radiative processes between the ion and the solid, through which electron states of the ion are filled. They also include resonant ionization, through which an electron from the ion occupies a state in the solid. In **Auger neutralization**, an electron from the solid occupies a state of the ion while another electron from the solid absorbs the energy difference and is emitted. **Auger de-excitation** describes the interaction of an outer-shell electron of the ion with a valence electron of the solid. As a result, the electron of the ion de-excites and the valence electron is emitted, or vice versa. In both scenarios the de-excited electron fills a low-energy state of the ion. Other de-excitation mechanisms of the ion are **autoionization** and **radiative decay**. They lead to electron and photon emission, respectively, and do not involve an atom of the solid.

The described models for electron de-excitation in a hollow atom face a bottleneck problem, since experiments showed that ion neutralization happens too fast in order to be explained by consecutive de-excitation processes [1, 11, 28]. The model of *Interatomic Coulombic Decay* (ICD), also called two-center Auger de-excitation, offers an explanation for such fast neutralization processes [29]. A core state of the ion is filled by an electron from a higher state while a virtual photon transfers the energy difference to an electron of a nearby atom, causing the electron to be emitted. This process is similar to Auger de-excitation shown in Figure 1(c), and it is sketched in Figure 2.

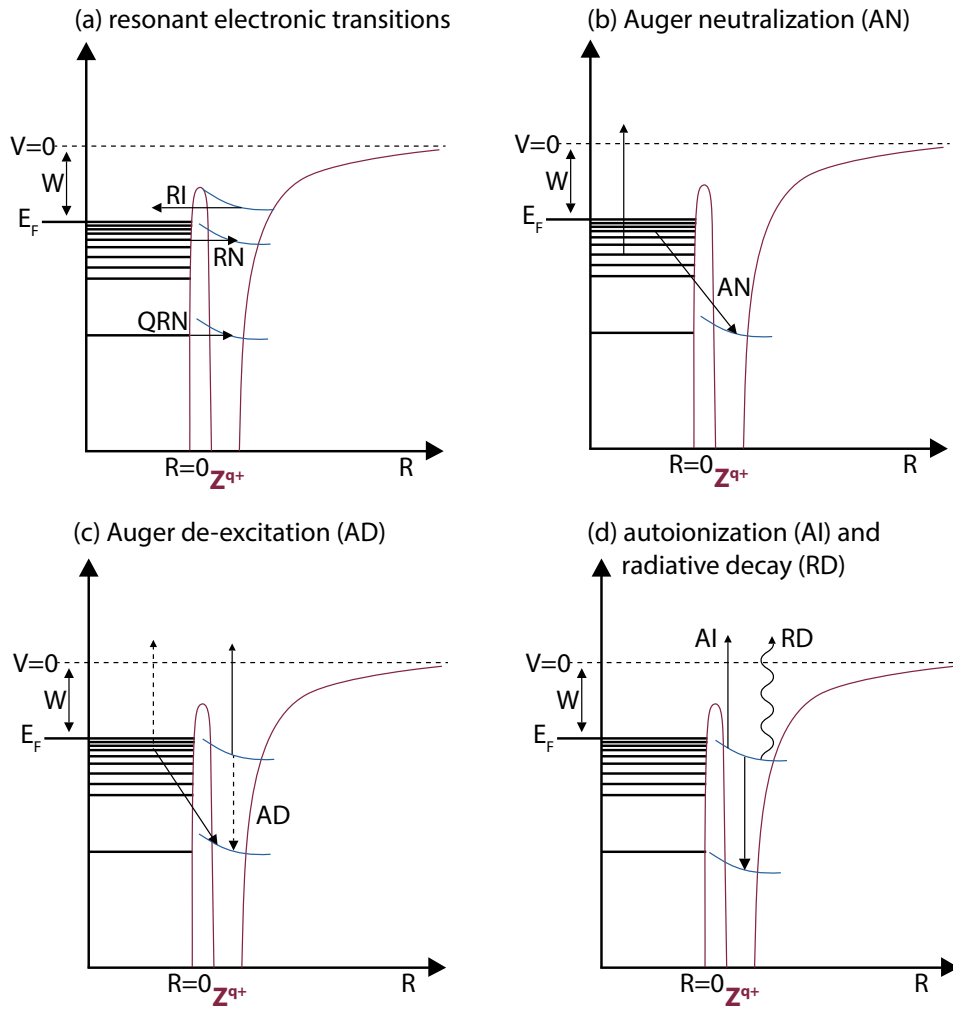


**Figure 1:** De-excitation and neutralization mechanisms for atoms, each one annotated in the corresponding title. RI: resonant ionization; RN: resonant neutralization; QRN: quasi-resonant neutralization. Adapted from [26, 27].

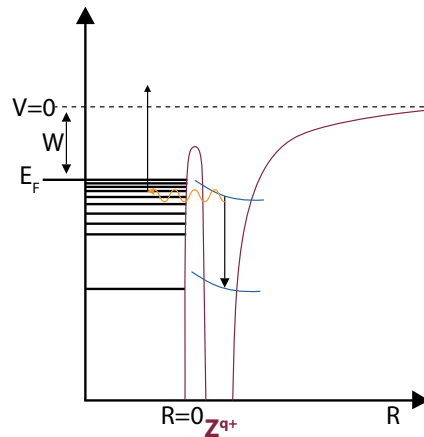


**Figure 2:** Depiction of the Interatomic Coulombic Decay allowing ultrafast de-excitation rates for hollow atoms. An outer-shell electron of the hollow atom de-excites and releases its energy in the form of a virtual photon (orange). This photon then transfers its energy to an electron of a nearby solid atom. The electron is emitted if its total energy is higher than vacuum level.

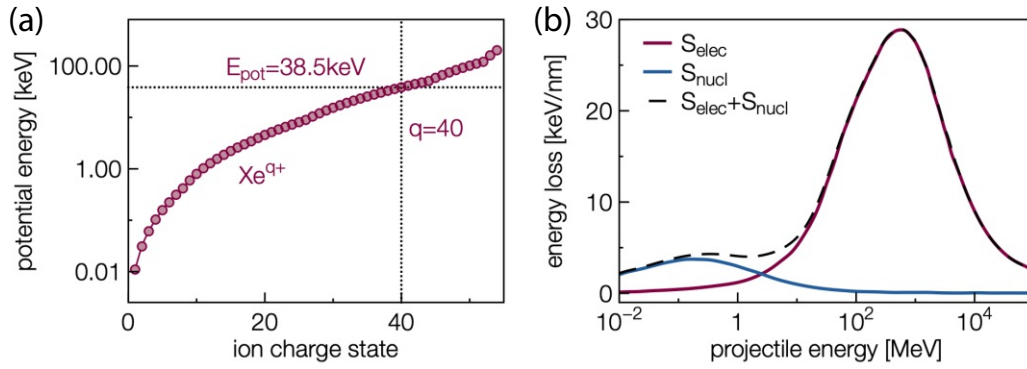


**Figure 3:** (a) Potential energy of a Xe ion as a function of its charge state. (b) Electronic and nuclear stopping power of Xe atoms in SrTiO<sub>3</sub> as a function of the projectile energy, calculated with the SRIM code [33]. Figure adapted from [34].

Through ICD, the fast de-excitation rates of hollow atoms at the order of  $10^{15} \text{ s}^{-1}$  can be explained [30]. The ICD process is limited to small distances between the two involved atoms, since the interaction strength falls off quickly with the interatomic distance  $R$ , particularly as  $\sim 1/R^6$ , which has also been confirmed by others [31,32].

If the ion itself is not scattered off the surface but enters the solid, it deposits its energy through electronic and nuclear stopping, and is eventually implanted. The sum of the electronic and nuclear contributions is the stopping power  $S$ , which is defined as the energy loss per distance traveled:

$$S = -\frac{dE}{dx} = S_e + S_n.$$

The stopping power acting on the ion depends on its kinetic energy and charge state. Figure 3 shows the potential energy of Xe<sup>q+</sup> ions for different charge states  $q$  as well as the calculated stopping power for Xe atoms in SrTiO<sub>3</sub>. It can be seen that nuclear stopping typically dominates at low energies for heavy ions. It subsides at higher ion energies while electronic stopping increases until its maximum, which is usually much higher than the one of nuclear stopping [35]. For light ions, nuclear stopping contributes only very little to the stopping and only at very low ion energies.

During the stopping process, the ion continuously captures electrons from the solid. Its average charge throughout the whole process is called the *equilibrium* or *effective* charge state, which can be estimated by

$$Z_{\text{eff}} = Z \left( 1 - e^{-\frac{v}{v_0} Z^{-2/3}} \right)$$

with the initial ion charge state  $Z$ , the ion velocity  $v$ , and  $v_0 = \frac{c}{\alpha} = 2.19 \times 10^6 \text{ m/s}$  being the Bohr velocity.

### 1.3 2D materials and motivation

The interaction of ions with 2D materials involve alterations to the aforementioned mechanisms. For example, the ions have a high chance of passing through the material and keep on traveling in forward direction. Any kinetic effects, such as kinetic electron emission, are also limited to the forward direction due to conservation of

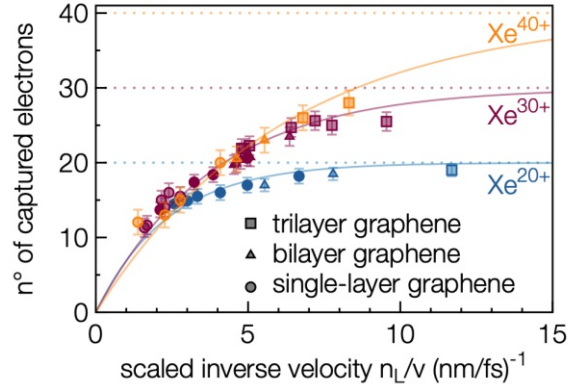


**Figure 4:** The number of captured electrons by  $\text{Xe}^{q+}$  ions ( $q \in \{20, 30, 40\}$ ) during multiple irradiation of single-, bi-, and trilayer graphene at varying kinetic energies. The data are given as a function of the scaled inverse velocity of the ions, where the scaling factor  $n_L$  equals the number of graphene layers in the sample. Adapted from [36].

momentum: Collision cascades inside 2D materials consisting of up to a few atomic layers will not be able to turn the momentum around.

Due to the small sample width, interaction durations of ions with 2D materials are on the fs scale [30]. This implies that the ions capture fewer electrons compared to interactions with bulk material. Consequently, most of the ions do not fully neutralize, but they end up in a certain distribution of exit charge states and kinetic energies after transmission. Measuring these using ion spectroscopy allows calculating the charge exchange and the energy loss of the ions in the material.

In general, such spectroscopy of highly charged ions transmitted through 2D materials not only provides insight into the interaction mechanisms between the ions and the material, but also information about the materials themselves. For example, electrons captured by the ion or emitted due to ICD lead to a positive charge patch in the material. Depending on the electronic properties and structure of the material, this patch vanishes quickly due to high electron mobilities, or it might lead to a Coulomb explosion and subsequent rupture of the material. While graphene stays intact during irradiations with 180 keV  $\text{Xe}^{40+}$  ions [11], similar irradiation settings cause nm-sized pores in carbon nanomembranes due to the comparably low electron mobility [5, 6].

Thus, for a better understanding of the electronic properties, the number of electrons captured and emitted from the material during the interaction with ions are important information. Highly charged Xe ions typically capture 10–30 electrons during their interaction with graphene, depending on their charge state and velocity. The number of captured electrons also increases with increasing graphene layer count [36]. Interestingly, the number of captured electrons show a uniform behavior as a function of the inverse velocity, if the latter is scaled by the number of graphene layers (see Figure 4). These results were calculated from the measured exit charge states of the transmitted ions.

The amount of emitted electrons correlates with the number of captured ones and thus also depends on the incident ion charge state, as shown in Figure 5. In contrast to the number of captured electrons, emitted electrons can be measured

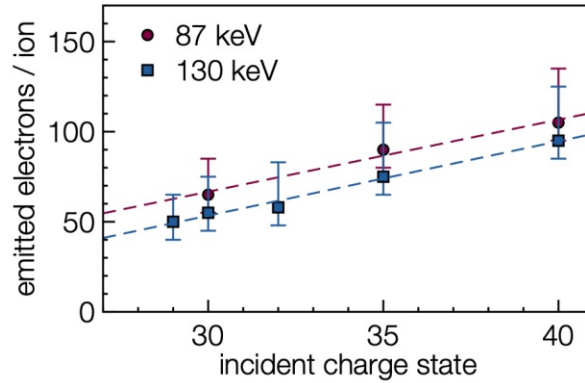


**Figure 5:** The number of emitted electrons from single-layer graphene, given for various incident Xe ion charge states and for two kinetic energies. Adapted from [37].

directly, for example with an electron statistics setup described in [22]. The results show an increase in emitted electrons per incident ion from 40 to around 100 for ion charge states 30 to 40, respectively. Moreover, a dependence on the kinetic energy of the ions can be seen. The electron yield increases for decreasing kinetic energy due to the increased interaction duration.

Lastly, the energy distribution of the electrons emitted from 2D materials is also significant information which has yet to be measured accurately. Especially low-energy electrons are of high interest, since the ICD model predicts an abundant emission during the interaction of highly charged ions with 2D materials [38]. Preliminary measurements using opposing electrostatic fields yielded a first assessment that the majority of the emitted electrons possess energies below 20 eV [39]. As is described in this thesis, an energy analyzer is installed in order to conduct these measurements with higher accuracy. Research using this analyzer will not only reveal the general energy distribution of the emitted electrons. It will also be used to investigate how parameters like the kinetic energy of the ions, their charge state, and the angle of incidence influence the energy distribution. Furthermore, different target materials might emit electrons with differently distributed energies as well, suggesting future measurements using bi- and trilayer graphene as well as other 2D materials like MoS<sub>2</sub>.

## 2 Experimental Methods

### 2.1 Hemispherical analyzer

#### 2.1.1 General description

Hemispherical energy analyzers (HEAs) are used for the energy-resolved detection of charged particles, for example electrons from X-ray Photoelectron Spectroscopy (XPS) or positively charged ions from Ion Scattering Spectroscopy (ISS). The HEAs described here are 180° spherical deflectors which consist of two concentric hemispheres with radii  $R_1$  and  $R_2$  ( $R_1 < R_2$ ), as well as an entrance and an exit slit for the particles. Figure 6 shows a sketch of the basic design of a hemispherical analyzer. Two different, constant voltages  $V_1$  and  $V_2$  are applied to the inner and outer hemisphere, respectively. The resulting electric field deflects charged particles, with

$$V(r) = V_0 - \left( \frac{\Delta V R_1 R_2}{R_0(R_2 - R_1)} \right) \left( 1 - \frac{R_1 R_2}{r} \right)$$

being the potential at radius  $r$  from the center of the hemispheres [40]. The potential along the mean radius  $R_0 = \frac{1}{2}(R_1 + R_2)$  is called  $V_0$ , and  $\Delta V = V_2 - V_1$  is the voltage difference between the two hemispheres. If the kinetic energy of a particle entering the analyzer is the same as the *pass energy*  $E_{\text{pass}}$ , it follows a semicircle with radius  $R_0$  and successfully leaves the analyzer through the exit slit. The pass energy is  $E_{\text{pass}} = -qk\Delta V$ , with the projectile charge  $q$ , the aforementioned voltage difference  $\Delta V$ , and

$$k = \frac{R_1 R_2}{R_2^2 - R_1^2} = \frac{R_1 R_2}{2R_0(R_2 - R_1)} \quad (1)$$

being the device-specific calibration constant [40].

Due to the finite size of entrance and exit slit, particles whose kinetic energy lies within a certain range centered around the pass energy will also successfully traverse the hemisphere, limiting the resolution of the HEA. The analyzer resolution is inversely proportional to the pass energy, i.e. reducing the pass energy increases the resolution. On the other hand, increasing the pass energy increases the intensity

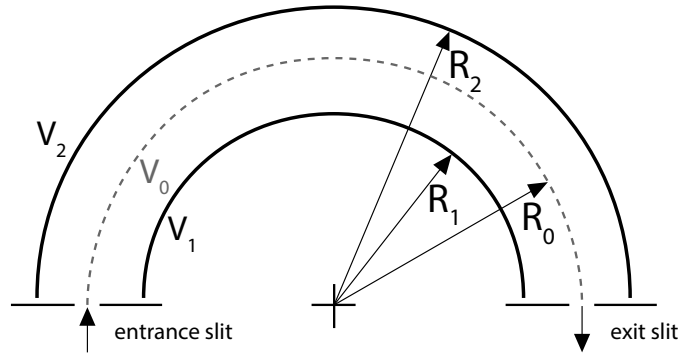


**Figure 6:** A sketch of the basic design of a hemispherical analyzer, consisting of two concentric hemispheres with different radii  $R_{1,2}$  and applied voltages  $V_{1,2}$ . The entrance and exit slits are connected by a semicircular trajectory with radius  $R_0$  and the potential  $V_0$  along it. Adapted from [40].

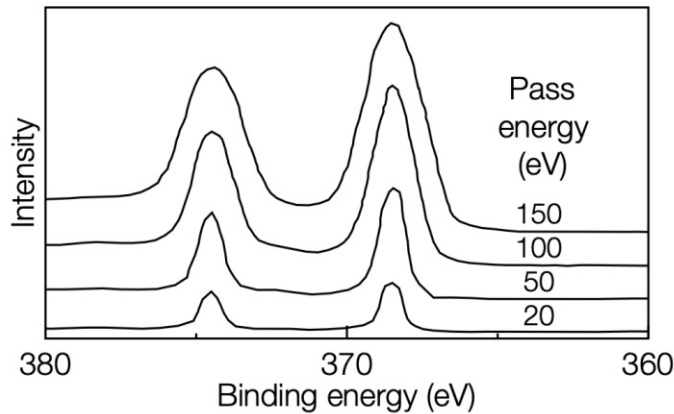


**Figure 7:** The Ag 3d part of an XPS spectrum measured at four different pass energies. The signal intensity increases with increasing pass energy but the resolution decreases. Adapted from [41].

of the measured signal. This can be advantageous for distinguishing the particle signal from background noise. As a result, increasing the pass energy results in more intense but wider (lower resolution) peaks, as shown in Figure 7.

HEAs are typically used to detect particles emitted from an irradiated sample and are able to catch all particles emitted into a certain area of the solid angle. Angle-dependent measurements can be conducted by varying the orientation of the sample relative to the HEA. The particle beam entering the analyzer is trimmed into circular shape by the opening and is thus well suited for being adjusted with electrostatic lenses. Modern HEAs typically contain an upstream lens system (a *transfer lens*) before the hemispherical part in order to accelerate or retard the incoming particles to the pass energy. This allows using a smaller pass energy and thereby increase the resolution of the analyzer. With a lens system, the analyzer has a fixed operating distance at which the sample should ideally be placed. Gradually changing the voltages to the lens system and plotting the measured counts creates a spectrum of varying particle energies.

In general, an HEA is operated in one of the two following modes [41]:

- Constant Analyzer Energy (CAE): the pass energy and thus the voltage difference between the two hemispheres is held constant. This implies a constant resolution across the whole measured spectrum. CAE is mostly used in XPS and Ultraviolet Photoelectron Spectroscopy.
- Constant Retardation Ratio (CRR): the pass energy is always set to be a certain fraction of the initial kinetic energy of the electrons  $E_{\text{pass}} = E_{\text{kin}}/b$ , with the retardation ratio  $b$ . Consequently, the two hemisphere voltages are changed by different amounts when measuring a range of particle energies. This also implies that the resolution of the analyzer depends on the chosen retardation ratio and the kinetic energy of the measured particles. On the other hand, signals of particles with low kinetic energies are suppressed, which makes CRR well suited to be used in ISS and Auger Electron Spectroscopy.

To count the particles which have successfully traversed the analyzer, a detector (usually an electron multiplier) is placed after the exit slit. One technical realization

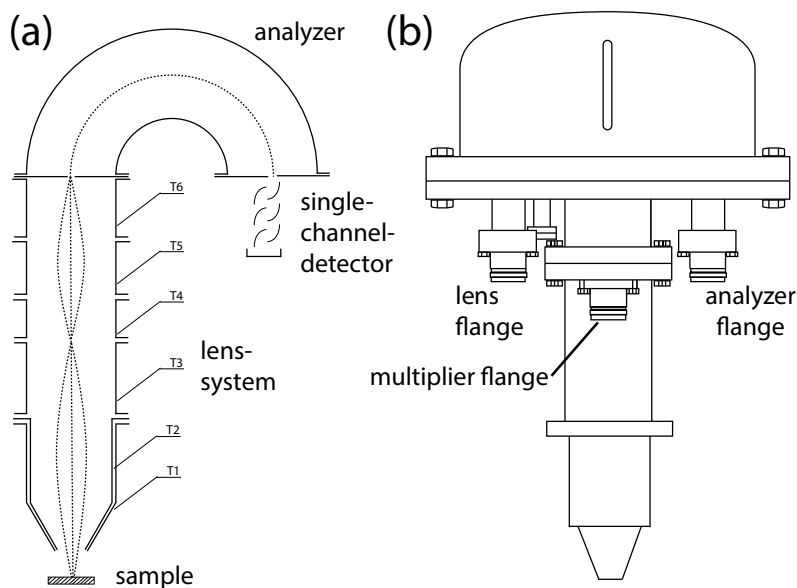


**Figure 8:** Sketches of the EA10+ showing (a) a simplified view of the interior and (b) an outside view. The sketches have been adapted from the EA10+ manual. Note that the lens and analyzer flange labels are swapped compared to the manual, since they are incorrectly annotated there.

of such a multiplier consists of multiple dynodes, to which tiered voltages are applied. If a particle with enough energy hits a dynode, multiple secondary electrons are emitted. These secondary electrons are in turn accelerated toward the next dynode due to the difference in the applied voltages. After a certain number of these multiplication steps, the resulting cloud of electrons creates a short current pulse, which represents a single detected particle. The number of detected particles can thus be measured by counting the number of pulses with an arbitrary counting unit.

### 2.1.2 SPECS EA10+

The HEA used for the electron measurements in this thesis is the *Energy Analyzer 10 Plus*, or EA10+, which was manufactured by SPECS<sup>1</sup>. Figure 8 shows sketches of the EA10+ internal structure and the connection plugs. A drawing of the EA10+ including the dimensions is provided in Figure 48 in Appendix A. The radii of the two analyzer hemispheres are  $R_1 = 80$  mm and  $R_2 = 114$  mm, respectively, resulting in a mean radius  $R_0 = 97$  mm for the central trajectory. All internal parts of the analyzer are surrounded by a  $\mu$ -metal shielding to prevent external magnetic fields from influencing the particle trajectories. The operating distance of the EA10+ is 23 mm, and a channeltron is used as electron multiplier.

The electronic components for the EA10+ consist of five units, three of which can be mounted inside a 19" rack. These three are the high voltage amplifier (HVA), the multiplier power supply (PS-SEV), and the energy analyzer power supply (PS-EA10N), and they are shown in Figure 9. The detection mode (XPS or ISS) can be set for each unit via respective controls, whereby all of them should obviously always be set to the same one. The XPS setting is used for measuring electrons, as it was

<sup>1</sup><https://www.specs-group.com/>



**Figure 9:** The front panels of the three rack-mounted electronic units of the EA10+. From top to bottom, the high voltage amplifier, the multiplier power supply, and the energy analyzer power supply are shown. The defined parameters are the ones which are automatically set by default when the units are turned on.

done throughout the work described in this thesis. Neither the remote control of the units nor any inter-unit remote connections were used.

**High voltage amplifier (HVA)** The HVA provides the necessary high voltages for the analyzer. The detection mode (ISS or XPS) defines the polarity of the voltages and thus the type of detected particles. A *sweep* or *control* voltage within 0 to +10 V is applied to input sockets of the HVA and then amplified by an adjustable gain factor. The gain is set by choosing one of three *range* values: 0.2, 2.0, or 2.6 kV, which correspond to the gain factors 20, 200, and 260, respectively. The amplified sweep voltage defines the energy of the electrons which can successfully pass the lens system and the hemispheres and will therefore be detected. For example, setting the HVA range to 0.2 kV and applying a sweep voltage of 5 V leads to the measurement of 100 eV electrons. In a generalized form, electrons with a kinetic energy of

$$E [\text{eV}] \hat{=} \frac{(\text{sweep voltage} [\text{V}])}{10 \text{ V}} \cdot (\text{HVA range} [\text{V}])$$

are detected. During the test and calibration phase of this work (Section 2.2), electrons with up to 200 eV were measured both with the 0.2 and the 2 kV HVA range. The latter was used to verify its functionality as well as to double check the electron peaks measured with the 0.2 kV HVA range.

The third input of the HVA is the *work function*, which is used to manually compensate for the different work functions of the sample and the analyzer, the latter being the one of graphite. The work function control can be set to any value from 0 to +10 eV. If it is set to a value greater than zero, the amplified sweep voltage is simply offset by this value, thus shifting the measured electron peaks to their correct position representing the actual kinetic energy of the electrons. The work function control was left at 0 eV for all measurements described in this thesis since only electrons from tungsten, gold, and graphene were measured, whose work functions are nearly the same as the one of graphite.

**Multiplier power supply (PS-SEV)** The multiplier power supply is responsible for supplying the high voltage for the multiplier. This multiplier voltage can be set to any value up to more than 3kV via a potentiometer. The so-called *conversion voltage* defines the energy of the electrons when they hit the first dynode of the multiplier. According to the manual, the conversion voltage for XPS is typically set to

$$\begin{cases} 250 & E_{\text{pass}} \leq 50 \text{ eV} \\ 200 + E_{\text{pass}} & E_{\text{pass}} > 50 \text{ eV} \end{cases}$$

with the pass energy  $E_{\text{pass}}$ . This ensures that the number of secondary electrons emitted from the first dynode is as high as possible, that the electrons are not decelerated too much, and that the electric field itself is not too high such that it would have a negative impact on the measurement quality. The set multiplier voltage limits the maximum possible conversion voltage and is thus always adjusted first. If the conversion voltage is increased too much for the currently set multiplier voltage, an associated ERROR-LED lights up.

It was noticed that counts were measured with the EA10+ even when the electron sources were turned off. These *dark counts* were only observed above a certain multiplier voltage threshold around 2.0kV, and their frequency rose with increasing multiplier voltage. They are presumably caused by field emission at the entrance of the channeltron. The measurements described in this thesis typically happened at multiplier voltages around 2.5 to 2.8kV.

**Energy analyzer power supply (PS-EA10N)** This power supply is the central control unit and is responsible for applying the appropriate voltages to the lens and analyzer systems. Instead of a single deceleration lens, as it was introduced before, the EA10+ has a more complex lens system consisting of six separate parts. These parts form two electrostatic lenses, with the first one acting as an einzel lens with a magnification factor of 2. The second lens is responsible for accelerating or retarding the incoming particles. The voltages applied to the lens system are automatically adjusted by the PS-EA10N in such a way that the electrons, which possess the kinetic energy defined by the applied sweep voltage, can successfully pass the lens system and are accelerated or retarded to the pass energy. Thus, they pass the hemisphere following the central trajectory and are detected by the electron multiplier. As mentioned before, electrons within a certain energy interval around the pass energy can also successfully traverse the hemisphere and widen the measured line in the spectrum. The resolution of the EA10+ is

$$\frac{\Delta E}{E_{\text{pass}}} = 2.5 \cdot 10^{-2}.$$

The main inputs of the PS-EA10N are for defining the pass energy of the electrons (called *transmission* energy on the device) as well as the operation mode. The constant  $k$  (see Equation 1), which is used in the pass energy formula  $E_{\text{pass}} = -qk\Delta V$ , turns out as  $k = 1.383$  for the EA10+. If the operation mode is set to  $\Delta E = \text{const.}$  (CAE), the pass energy can be adjusted to any value from 0 to 199.95 eV in steps of 0.05 eV. On the other hand, if the chosen mode is  $\Delta E/E = \text{const.}$  (CRR), the pass energy cannot be changed and the display only shows the selected retardation ratio instead ( $b \in \{3, 10, 30\}$ ).

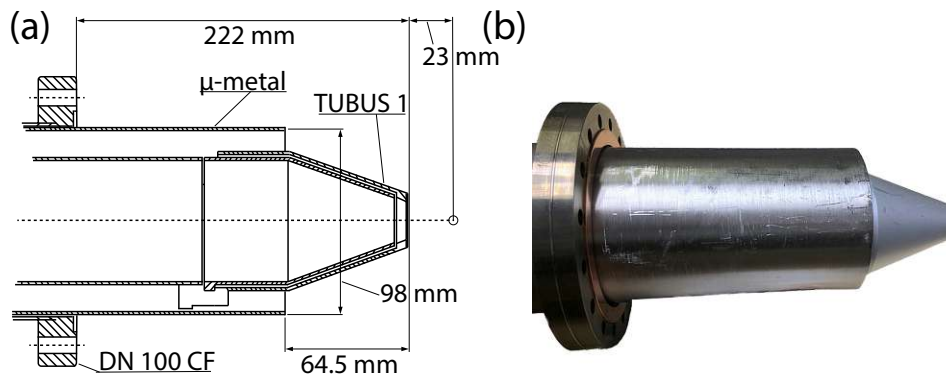


**Figure 10:** (a) Sketch of the foremost part of the EA10+, adapted from the manual. Note that the distance from the CF100 flange to the front end of TUBUS 1 is 222 mm instead of the 173.5 mm given in the manual. (b) Photo of the same part of the real device.

The third parameter of the power supply is the amplitude of a sinusoidal signal which is used to modulate the voltage applied to the analyzer. During the measurements conducted for this thesis, the modulation was always set to 0. The fourth and final parameter is for the TUBUS 1, the foremost part of the hemisphere, which is shown in Figure 10.

The TUBUS 1 can be set to one of the following modes:

**work function** TUBUS 1 is set to the same voltage as the *work function*, which is defined at the HVA.

**electrometer** TUBUS 1 is disconnected from any voltage source and can therefore be used to measure the current of impacting particles. This is preferably done with a bias of up to +90 V in order to prevent measurement errors due to collision-induced secondary electron emission. This setting unfortunately does not work. This is due to a fault in the electronics, since the current can still be measured directly at the TUBUS 1 pin at the lens flange.

**ground** TUBUS 1 is grounded.

**variable** The voltage applied to TUBUS 1 can be manually set to a custom value from  $-46$  to  $+46$  V via a separate potentiometer.

**Coupling plug (SI-COP) and preamplifier (UNI-PAH)** The remaining two electronic units are the coupling plug (SI-COP) and the preamplifier (UNI-PAH), which are shown in Figure 11. The coupling plug is directly connected to the multiplier output plug of the analyzer and decouples the pulses from the electron multiplier. The preamplifier in turn is directly connected to the coupling plug and amplifies its output signal. The multiplier power supply (PS-SEV) provides the power for the preamplifier, which outputs the amplified electron pulses in the form of positive TTL signals with  $50\ \Omega$  impedance. Figure 12 shows an example of such a pulse. To measure the number of detected electrons, an analog counting unit can be used to display the number of output pulses. Another possibility is to process the counts further, e.g. with a counting unit which averages the counts over a certain period of time and forwards the result to a PC in the form of a digital signal.

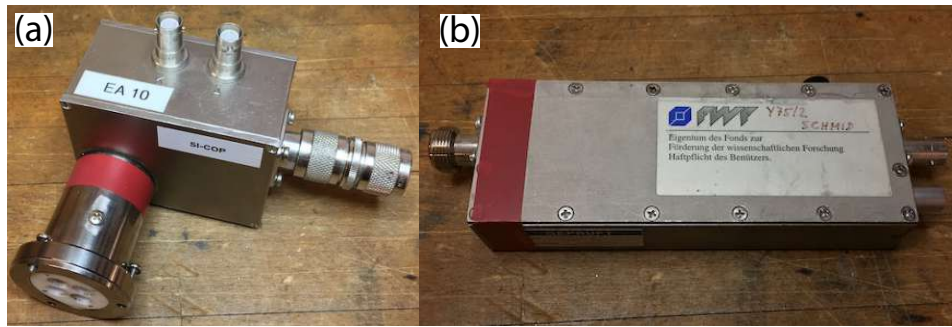


**Figure 11:** (a) The coupling unit SI-COP, and (b) the preamplifier UNI-PAH.

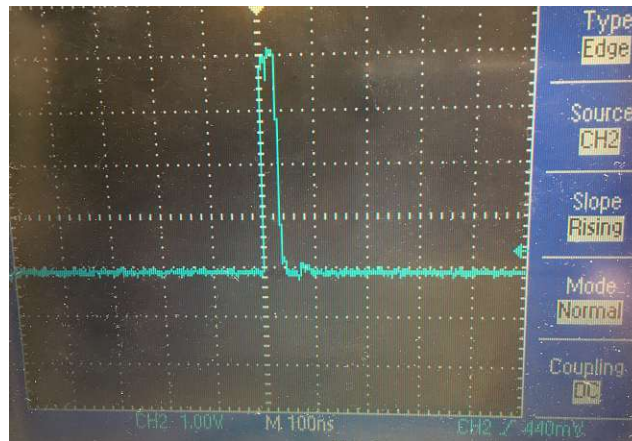


**Figure 12:** A single output pulse of the preamplifier measured with an oscilloscope. The peak voltage of the pulse is around 4 V, the peak width is 50 ns.

**Connection diagram** For a complete overview of all the electronic units of the EA10+, their connection diagram is shown in Figure 13.

**Digital version** To plan the positioning of the HEA, a digital version of the analyzer was created using the CAD software SolidWorks<sup>2</sup>. Since the HEA is mounted horizontally to the side of NIELS about 1.4 m above the floor, it needs a supporting structure. The structure is made up of item<sup>3</sup> parts and was also designed digitally. Not only is the structure used for supporting the HEA, but it also provides space for the necessary electronics to be mounted in a rack underneath the analyzer itself. The supporting structure is designed to be directly attached to the existing item parts of NIELS. A render of the digital versions of the HEA and its supporting structure attached to NIELS are shown in Figure 14.

Initially, two different ways of connecting the HEA to its supporting structure were designed (see Figures 49 and 50 in Appendix A). In the end, only the second one was used because it provided more stability as well as an additional, second degree of freedom for positioning the HEA horizontally.

<sup>2</sup><https://www.solidworks.com/>

<sup>3</sup><https://www.item24.de>

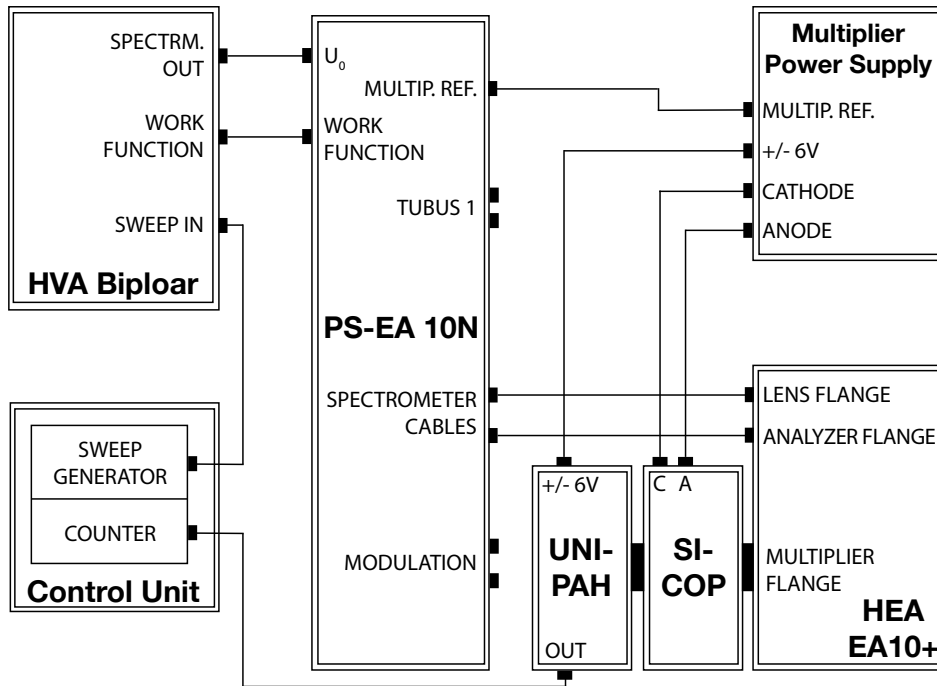


**Figure 13:** The connection diagram of the EA10+ electronic units. The remote connections have been omitted since they were not used. Adapted from the manual.

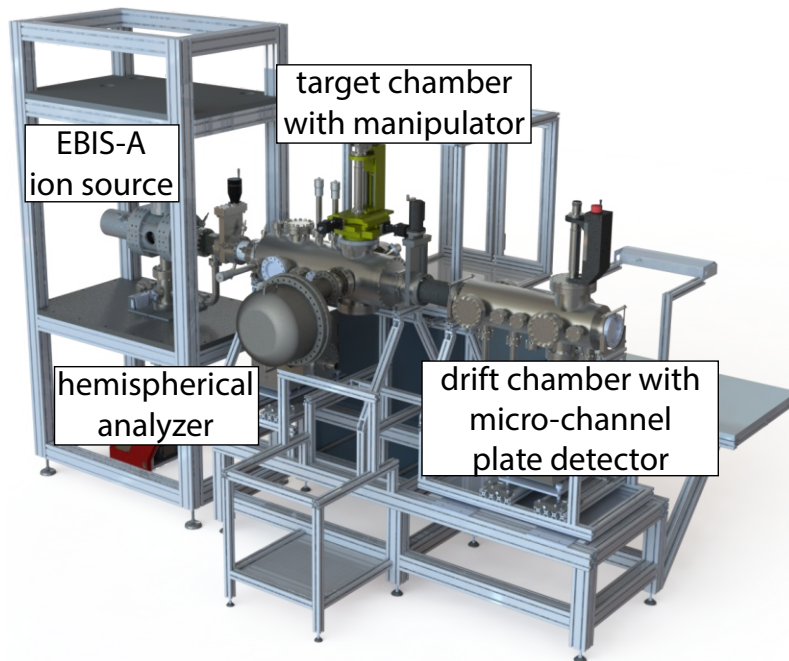


**Figure 14:** A render of the digital version of NIELS with the attached EA10+ and its supporting structure.

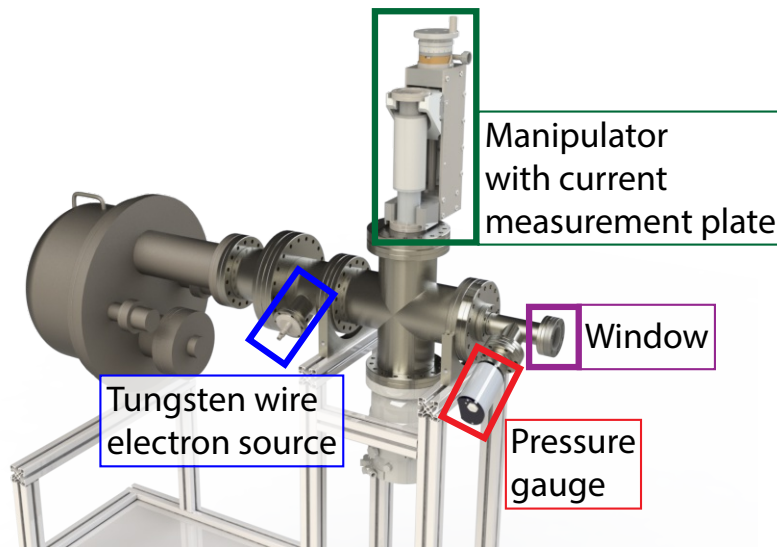


**Figure 15:** Render of the ultimately used test rig setup with a tungsten wire as electron source, placed directly in front of the opening of the hemispherical analyzer.

## 2.2 Test rig

### 2.2.1 Experimental setup

The EA10+ had not been used for many years and preliminary tests were planned before it was mounted to NIELS to carry out measurements. The supporting structure of the HEA was designed in such a way that it could simply be extended by a few additional item parts. These modifications allowed the HEA to stand on its own while being attached to the test rig. Figure 15 shows a depiction of the setup. A drawing of the setup including the dimensions is provided in Figure 51 in Appendix A.

The central part of the test rig consisted of a 4-Way cross which the HEA was connected to. A turbomolecular pump was connected to the bottom flange of the 4-Way cross while the top flange was used to connect a manipulator. The remaining flange served as a way to connect a pressure gauge.

To measure the electron current inside the test rig, a  $5 \times 5$  cm steel plate was mounted to the manipulator in an electrically insulated way and connected to a feedthrough pin with a wire. Electrons hitting the plate induced a current which was measured outside the test rig using a picoammeter. To minimize measurement errors due to secondary electron emission, the plate was occasionally positively biased.

A basic power supply was used to manually set the sweep voltage of the HEA. Manually adjusting the sweep voltage using the potentiometer of the power supply was relatively inaccurate and made it very difficult to find the exact electron peak. Thus, the sweep voltage was only set through this power supply to check the order of magnitude of measured electrons and to verify the approximate position of an expected electron peak. To find an exact electron peak position and measure the counts there, a script which automatically measures a spectrum was created (Section 2.2.2).

On the test rig, a tungsten wire was used as the source of electrons. It was simply connected to both pins of a CF40 flange with two BNC feedthroughs. A tungsten wire works as an electron source by passing a current through it to significantly raise

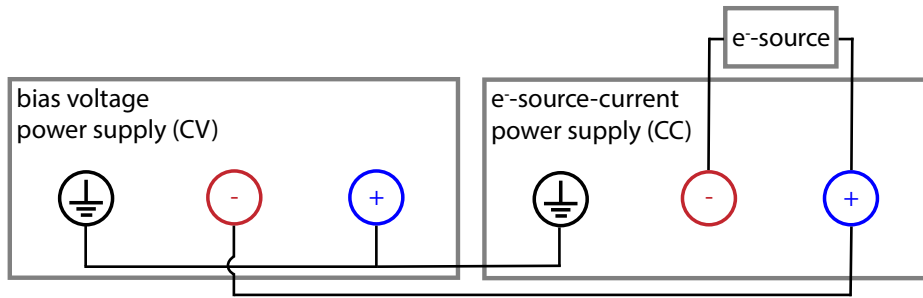


**Figure 16:** A sketch showing the setup to negatively bias an electron source, as it was used for the tungsten wire. The first power supply provides the bias voltage for the second power supply (CV: constant voltage). The second power supply is responsible for the current through the electron source (CC: constant current). This one has to withstand the bias voltage being applied to its inputs.



**Figure 17:** Photo of the tungsten wire feedthrough construct for the ultimately used test rig setup. It was constructed in such a way that the tungsten wire ended up right in front of the EA10+ opening.

its temperature and thus aid the field-extraction of electrons. Field-extraction is accomplished by applying a negative bias to the tungsten wire with a power supply. This bias simultaneously serves as a way to define the energy of the electrons with respect to ground. Figure 16 shows a connection diagram for the general setup of a biased power supply. The downside with using a tungsten wire is that it is not possible to focus the extracted electrons in any way. Nevertheless, tens to hundreds of pA could be measured on the positively biased plate.

The tungsten wire was placed directly in front of the HEA opening in order to maximize the amount of electrons which entered the HEA. The therefore constructed wire feedthrough setup is shown in Figure 17. The position of the feedthrough flange is shown in Figure 15.

### 2.2.2 Data acquisition

The secondary electrons of the electron multiplier in the HEA are output by the preamplifier in the form of voltage pulses. On the test rig, these pulses were counted with two dedicated counter units. The first one was an analog counter, which was used to monitor the measured counts. The second counter was a custom built unit which receives the analog signal as input, averages the counts over a set period of

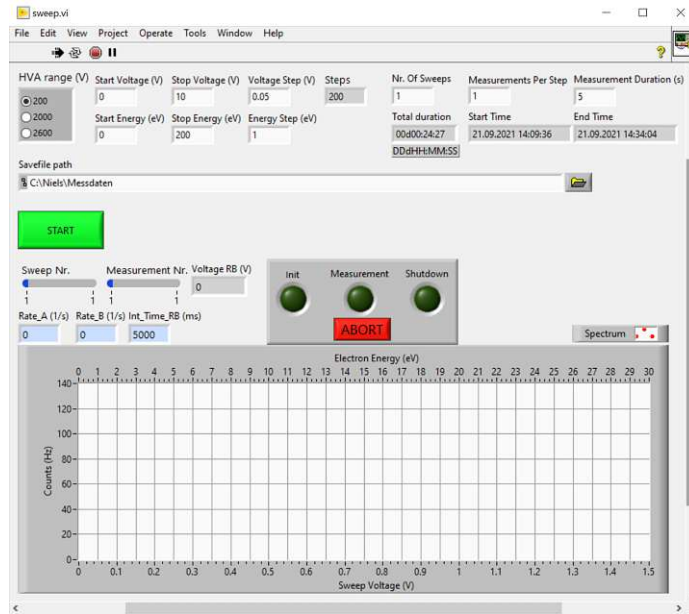


**Figure 18:** Screenshot of the LabView VI which was used for the automated spectrum measurements.

time, and outputs the average counts in Hertz to an ethernet port.

A LabView<sup>4</sup> program (also called *virtual instrument*, or VI) is used to read the output of the custom counter unit and display it. The program can also be used to set the integration time of the counter unit, i.e. over how much time the retrieved counts are averaged before they are returned. Another VI was used to control the output voltage of an ADC and thereby apply the sweep voltage to the HVA.

To measure electron spectra with the HEA, a new LabView VI was created which automatically carries out measurements (see Figure 18). After starting the program, the set HVA range is selected, which defines the scale of the other input values and the output graph. The desired lower voltage limit ( $V_{\text{start}}$ ) and upper voltage limit ( $V_{\text{stop}}$ ) of the spectrum set the overall range of the applied sweep voltage anywhere from 0 to 10 V. The voltage step ( $V_{\text{step}}$ ) defines how much the sweep voltage will be increased after each measurement step until  $V_{\text{stop}}$  is reached. Thus, the measurement of a complete spectrum consists of  $N_{\text{step}} = \lfloor (V_{\text{stop}} - V_{\text{start}}) / V_{\text{step}} \rfloor + 1$  steps. The voltage values are also simultaneously converted to electron energy (in eV) and displayed in their own, editable input fields. These fields can also be used to define the measurement ranges and step size in units of eV. Furthermore, it is possible to set the number of measurements at each voltage step ( $N_{\text{meas}}$ ), and how many times the whole spectrum is measured ( $N_{\text{sweep}}$ ).

The integration time of the custom counter unit ( $T_{\text{int}}$ ) is another parameter which has to be defined. The LabView VI of the counter intrinsically contains a total of 1 s of *wait* commands, and the main program also needs some time for processing and plotting the data at each step.

<sup>4</sup><https://www.ni.com/en-us/shop/labview.html>

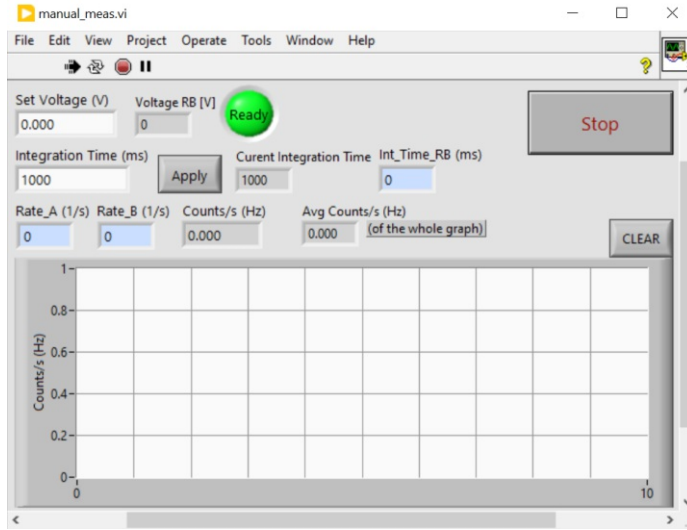


**Figure 19:** Screenshot of the LabView VI which was used for manually measuring the electron counts at a certain sweep voltage.

As a result, a fully measured spectrum takes about

$$t_{\text{tot}} = N_{\text{sweep}} \cdot N_{\text{meas}} \cdot N_{\text{step}} \cdot (T_{\text{int}} + 2 \text{ s}) + 10 \frac{\text{s}}{\text{V}} \cdot (N_{\text{sweep}} - 1) (V_{\text{stop}} - V_{\text{start}})$$

seconds to complete. The second part of the formula is the time required for changing the voltage back to  $V_{\text{start}}$  at  $-0.1 \text{ V/s}$  for each additional measured spectrum. The thereby estimated measurement duration as well as the start and end timestamps are displayed as a convenient way to plan measurements. Finally, the name of the text file has to be defined where the gathered measurement data will be saved. The first line contains the defined global parameters

$$V_{\text{start}}, V_{\text{stop}}, V_{\text{step}}, N_{\text{spec}}, N_{\text{meas}}, T_{\text{int}}, V_{\text{range}}$$

with the HVA range  $V_{\text{range}} \in \{0.2 \text{ kV}, 2 \text{ kV}, 2.6 \text{ kV}\}$ . The rest of the file consists of  $N_{\text{sweep}} \cdot N_{\text{meas}} \cdot N_{\text{step}}$  lines of comma-separated sweep voltage and measured counts:

$$V_{\text{sweep}}, N_e.$$

It has to be noted that if the measurement is ended early via the *Abort* button, all measured data up until this point is written to the file, but the parameters of the first line stay unchanged.

For measurements with multiple sweeps or measurements at each step, a Python script is used to aggregate the measurement data into a new file. This file consists of  $N_{\text{step}}$  lines, each one containing the sweep voltage and a set of data for it: the sum of the counts at the specific voltage, the sum divided by the number of sweeps, and the mean, median, and standard deviation of the measured counts.

To manually set the sweep voltage to a specific value and observe the detected electrons, another VI was created, which is shown in Figure 19. It was used to check the consistency of the average counts at a certain sweep voltage, and also to measure the change of the average counts with increasing multiplier voltage (Section 3.1).

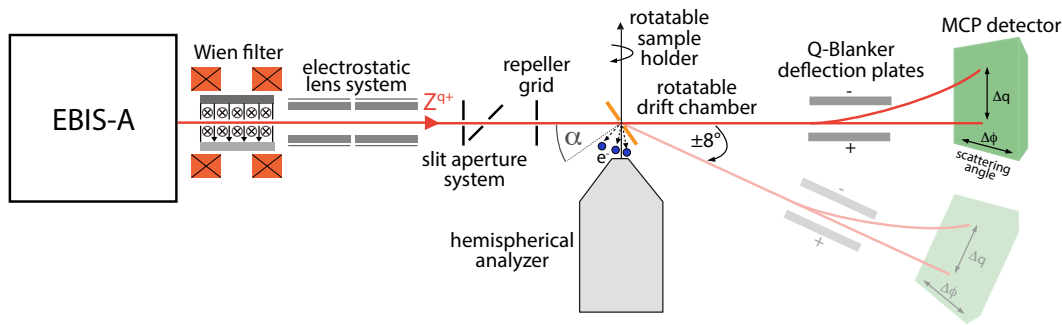


**Figure 20:** Sketch of the NIELS experiment showing an overview of the setup used for the measurements described in this thesis. The direction of the hemispherical energy analyzer and the drift chamber rotation are both out of plane. The angle  $\alpha$  is used to denote the angle of incidence for all measurements in this thesis. The repeller-grid was originally part of the electron emission statistics setup and is here used to keep ion pump electrons away from the hemispherical analyzer. Adapted from [42].

The adjustable parameters consist of the desired sweep voltage and the integration time of the counter unit. If the sweep voltage is changed, the program slowly adjusts it toward the desired voltage at  $\pm 0.1$  V/s. Pressing the *Apply* button sets the integration time of the counter unit to the given value. The program outputs both the measured counts and the average counts of the whole graph.

## 2.3 NIELS

### 2.3.1 General description

Neutral and Ion Energy Loss Spectrometer (NIELS) is an experimental setup for investigating the interaction of highly charged ions with 2D materials at the Institute of Applied Physics. What follows is a basic overview of NIELS. For a more detailed description, see [42]. Figure 20 shows an overview of NIELS including the ion beam path from the ion source up to the final detector.

The ions used in the described experiments are prepared in a DREEBIT Electron Beam Ion Source (EBIS-A). A beam of electrons collides with gas atoms (typically Ar or Xe) which are ionized in the process. The created ions are further ionized to higher states by successive collisions. Through these collisions,  $\text{Xe}^{q+}$  ions with charge states ranging from  $q = 1$  to  $q = 40$  are produced. Such high charge states are achievable because of the optimized ion confinement both axially, via three drift tubes, and radially by the negative space charge of the electron beam. An extraction electrode then forms the initial ion beam, whose ions possess kinetic energies from  $5 \cdot q$  keV up to  $10 \cdot q$  keV, depending on the applied voltages inside the ion source. Additionally, the whole ion source can be negatively biased in order to reduce the kinetic energy of the ions without changing the parameters of the source itself. However, any electrostatic lenses or deflection plates affecting the ion beam after it leaves the source have to be adjusted accordingly in order to keep the same beam profile and trajectory.

The ions first pass a Wien filter, which is used to select a certain charge state. Afterwards, an electrostatic lens system and a pair of slits define the shape of the ion beam in order to focus it onto the 2D sample in the target holder. The ions interact with the sample, pass through it, and end up as a distribution of exit charge

states and energies. The Q-Blanker, an electrostatic deflector consisting of two parallel plates, separates the different ion charge states spatially. This causes the ions to hit the subsequent micro-channel plate (MCP) detector at different vertical offsets. The MCP detects the individual ions and both their horizontal and vertical impact location. Consequently, the exit charge state of the ions is given by their vertical position on the MCP, while the horizontal impact location corresponds to the scattering angle within  $\pm 0.5^\circ$ . By rotating the whole drift chamber around the axis of the target holder, measurements at scattering angles up to a total of  $\pm 8^\circ$  are possible.

The energy of the detected ions is measured via their time-of-flight (TOF) from the sample through the drift chamber until they hit the MCP detector. Each TOF measurement requires associated start and stop signals. For the measurements described in this thesis, a detected ion on the MCP delivers the start signal, while an electron detected by the hemispherical analyzer serves as the stop signal.

During the interaction of the ions with the sample, various numbers of electrons are emitted. As described in this thesis, the newly added hemispherical electron analyzer is used to measure the electron energy distribution. Before the analyzer was put in operation, a positively biased grid collected the emitted electrons and they were measured on a semiconductor (Passivated Implanted Planar Silicon, PIPS) detector. Through this process, the number of electrons could be measured, but not their energy [22].

The investigated 2D samples need a supporting material, *Quantifoil*, which is a 10 to 20 nm amorphous carbon film. The Quantifoil itself is mounted on a gold TEM grid by which the samples are handled. Ions hitting the Quantifoil end up possessing less kinetic energy compared to the ones interacting with the sample, resulting in a longer TOF. Furthermore, the majority of these ions also fully neutralize in the Quantifoil and are thus not deflected by the Q-Blanker before hitting the MCP. Those two characteristics make it possible to differentiate ions which hit the Quantifoil from those which hit the sample. Ions hitting the gold TEM grid do not pass through it and are thus not detected by the MCP, but electrons are emitted in the process. To avoid measurement errors due to these electrons, *coincidence measurements* are carried out. This means that only electron events with time-correlated ion events on the MCP are taken into account, the others are discarded.

### 2.3.2 Experimental setup

Figure 14 on page 14 shows how the HEA is mounted to the target chamber of NIELS. The analyzer replaces the transfer chamber, thus the whole setup has to be vented for swapping samples until a new transfer chamber is added. This one will be constructed on top of the target chamber in the near future.

A newly designed  $\mu$ -metal shield surrounds the target holder and helps to avoid magnetic fields influencing the trajectory of low-energy electrons. A CAD render of the  $\mu$ -metal as well as a photo of the manufactured object are shown in Figure 21. The drawing including the dimensions is provided in Figure 52 in Appendix A.

Furthermore, a new, compact target holder had to be designed which fits inside the  $\mu$ -metal element (see Figure 22). It is small enough so that it can be rotated, which changes the angle of incidence of the ions and also guides the direction of the emitted electrons. Drawings of the two target holder parts including the dimensions

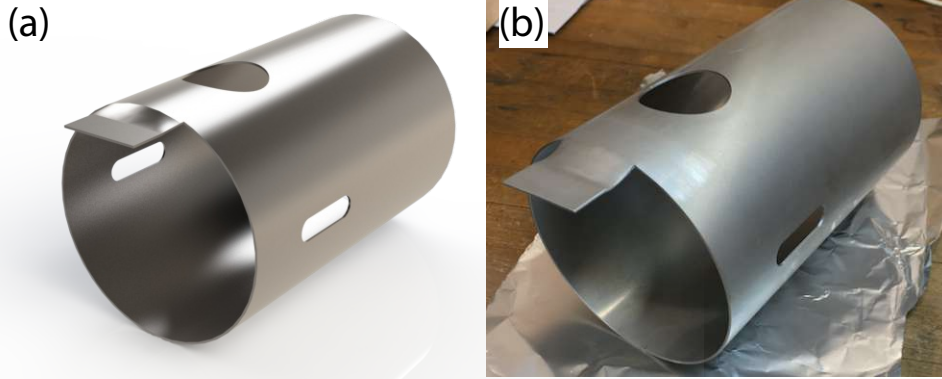


**Figure 21:** (a) Render of the newly designed  $\mu$ -metal shielding. (b) A photo of the manufactured object.

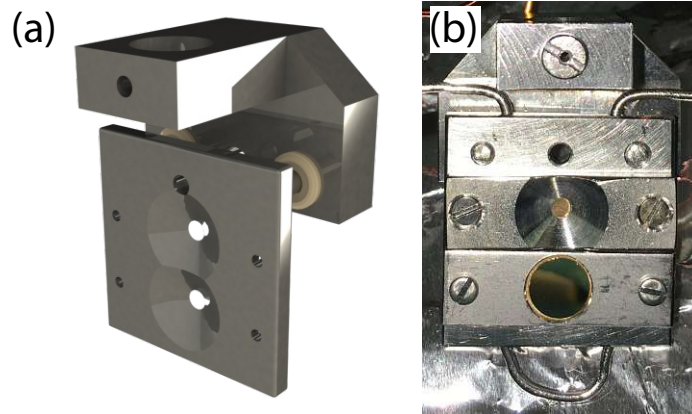


**Figure 22:** (a) Render of the newly designed target holder. (b) Photo of the target holder with two samples: single-layer graphene (TUW172) in the upper slot, and Au (111) (TUW100) in the lower slot.

are provided in Figure 53 and 54 in Appendix A. The target holder includes two bores for a 1NcI15 heating wire in order to heat up and thereby clean the samples. The plate can hold up to two samples and is mounted to a plate-holder in an electrically insulated way. The plate-holder in turn is mounted to the manipulator pole. By connecting a wire to the plate it is possible to measure the current of the ion beam. An additional hole through the plate and the plate-holder allows measuring the ions on the detector directly at the back of the chamber without any prior interactions. This is used for setting up the ion beam and the plate position. An inside view of the target chamber, both rendered and from a camera, is shown in Figure 23.

### 2.3.3 Data acquisition

As described before, the incoming ion beam hits the sample and the ions are then detected by the MCP. The method of coincidence measurements is applied in order to connect the electrons to the ions which caused their emission. This allows omitting electrons emitted by ions hitting the gold TEM grid. Additionally, electrons from the Quantifoil are removed from the spectrum by filtering the measured events by the TOF and the exit charge state of the ions, i.e. their vertical position on the MCP.

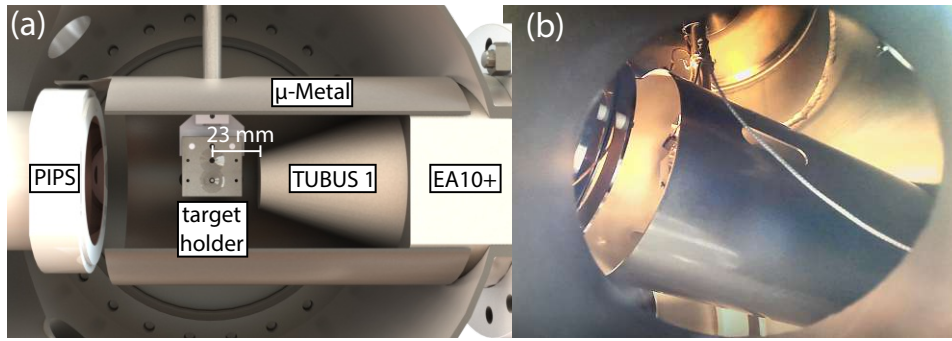


**Figure 23:** (a) A render showing a section view of the inside of the target chamber, with the new target holder, the  $\mu$ -metal shield, and the EA10+. The operating distance of the analyzer (23 mm) is marked with a small sphere, located directly at the lower sample spot of the target holder. (b) A photo taken with the camera mounted to a flange-window showing the inside of the target chamber.

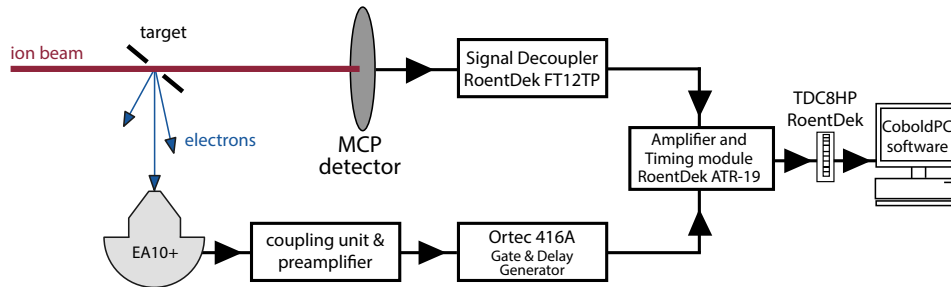


**Figure 24:** The electronics setup at NIELS for measuring electrons with the EA10+ in coincidence with the ions at the MCP detector.

For the test phase (Section 2.2) a LabView VI was created to measure electron spectra with a custom counter unit while gradually changing the applied sweep voltage. At NIELS, a new electronics setup was used, which is depicted in Figure 24. The counting was performed with the CoboldPC2011 software, optionally in coincidence with the detected ions: The positive TTL pulses of the HEA preamplifier are fed into an EG&G Ortec 416A Gate & Delay Generator unit in order to transform them into NIM logic pulses. They are then forwarded to the RoentDek ATR19 amplifier which communicates with Cobold. Setting the input trigger of Cobold to the ion signal enables measurements in coincidence with the electrons. If the trigger is set directly to the electron signal, non-coincident electron spectra can be measured, completely ignoring the ions.

A LabView VI still handles setting the sweep voltage, but instead of querying the count rate of the counter unit, it communicates with Cobold and orders it to count electron events. Sending commands from within LabView to Cobold is done by running the *CoboldPCCMD* executable followed by the particular command, i.e.

```
C : /Users/Niels/Desktop/CoboldPC/CoboldPCCMD.exe <command>.
```

The previously used LabView VI was extended by the required new features, a screenshot of the user interface is shown in Figure 25.

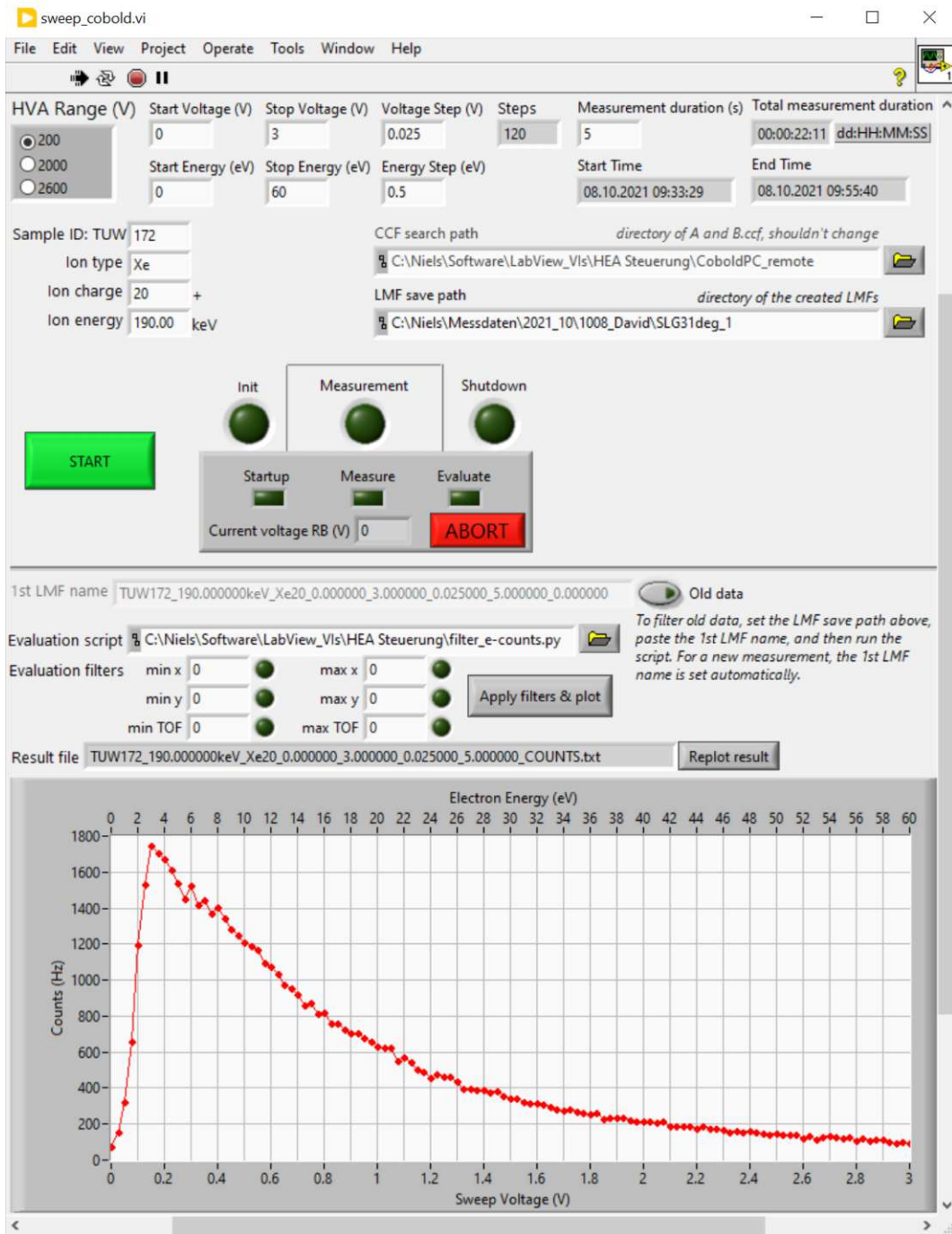


**Figure 25:** Screenshot of the LabView VI used for the measurements at the NIELS experiment using the RoentDek devices. Apart from the measurement settings, the interface also provides the possibility to filter the measured data and plot the resulting spectrum.

The communication with Cobold works as follows:

1. The command `setpath CCFPATH, <path>` is sent to Cobold to set the search path for the *Cobold Command* files (CCFs) which will be executed.
2. The command `setpath LMFSPATH, <path>` is sent to Cobold to define where the *List-Mode* files (LMFs) will be saved to.
3. At each step of the spectrum measurement, the following actions happen:
  - (a) The command `execute A.ccf` orders Cobold to execute the first of two CCFs. This CCF defines the basic parameters of Cobold for each measurement.
  - (b) Secondly, the command `new hardware, <name>, analysis` defines the name of the LMF which will be created by Cobold. The variable `<name>` contains the identifier of the sample, the irradiation parameters, the chosen sweep voltage settings, and the current sweep voltage.
  - (c) The command `execute B.ccf` runs the second CCF which starts the actual measurement. Cobold then creates a new LMF with the name defined in (b) in the LMF path and fills it with the measurement data.
  - (d) After waiting for *measurement duration* amount of seconds (defined in the LabView VI), the commands `remove update` and `stop` order Cobold to stop the measurement.
  - (e) The LMF written up to this point are evaluated by calling a Python script, which aggregates the measured counts for each sweep voltage, optionally restricted by user-defined filters. The spectrum is then plotted in a graph.

This workflow results in Cobold creating one LMF for each sweep voltage step. Thus, even after a completed measurement, it is possible to manually apply different filters to the gathered data and the graph is updated to show the resulting spectrum.

The described VI was used for measuring full electron spectra by setting the Cobold input trigger to the electron signal channel and thus not taking the ions into account. The main restriction of this VI is that the measurement duration has to be defined beforehand and is constant throughout the whole measurement. For coincidence measurements, the input trigger in Cobold is set to the ion signal channel. The number of electrons detected in coincidence with the ions is small, which is reduced even further by the small solid angle of the detector ( $\approx 10\%$ ) and also because only ions hitting a certain area of the MCP are taken into account. The latter discards neutral and singly charged ions, which stem from interactions with the Quantifoil, as well as fully charged ions which did not interact with any material by passing through pin holes (i.e.  $\mu\text{m}$ -sized holes in the sample).

Thus, using a constant measurement duration for each point in the spectrum is not feasible. Coincidence measurements were conducted manually at a few selected electron energies. In detail, this means that the electron energy is set via the VI shown in Figure 19 on page 18 and a prepared CCF is executed with Cobold. The acquisition is run until a peak in the TOF spectrum emerges. A Python script is then used to count the number of electron events in the LMF which are part of this TOF peak and also lie within a certain area of the MCP, thus limiting the exit charge state to those ions which interacted with the graphene.

## 3 Results and Discussion

### 3.1 Test phase

An extensive set of measurements was conducted on the test rig using a tungsten wire as electron source which was placed directly in front of the HEA opening. Power of around 7 W was applied to the wire for it to glow brightly. It has to be noted that the electron emission of the heated and biased tungsten wire was quite unstable. Therefore, the electron current was logged before and after each measurement using the steel plate inside the test rig. For the analysis of the measured data the spectra were then corrected by their respective plate current in order to allow for a direct comparison.

The first measurements were about the behavior of the counts when the multiplier voltage is increased. Figure 26 shows the average counts as a function of the multiplication voltage, measured at three different occasions and with two different bias voltages. The plots show that no counts are measured below 1.4 kV, and that they start increasing at that threshold. It then transitions into a plateau-like behavior above 1.6 kV until around 3 kV, where the counts steeply increase again. Therefore, the multiplier voltage was adjusted to values between 1.5 and 3.0 kV for the measurements described in this thesis.

Multiple HEA spectra were measured at different bias voltages ranging from  $-50$  to  $-200$  V, resulting in electrons with 50 to 200 eV kinetic energy. Each of these measurements was conducted with 190 eV pass energy, 0.2 kV HVA range, and a multiplier voltage from 1.5 kV up to 2.4 kV. Depending on the multiplier voltage, the conversion voltage was always set to either the highest possible value or  $200 + E_{\text{pass}}$ , whichever was lower. Figure 27 shows a few of the measured electron spectra at three different bias voltages, i.e. electron energies. It can be seen that the detected electron peaks are located at the expected electron energy and that the counts reduce

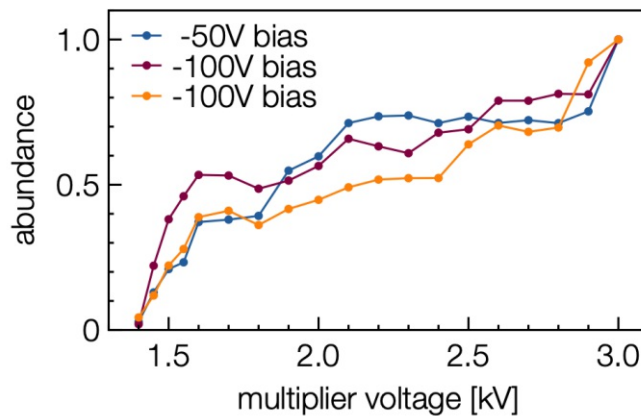


**Figure 26:** The abundance of measured electrons as a function of the applied multiplier voltage. A biased tungsten wire was used as electron source with a current of around 3 A passing through it. The measurements were conducted with 190 eV pass energy, 0.2 kV HVA range, and the sweep voltage was adjusted to the value with maximum count rate. The abundances were normalized to 1 since these three measurements happened at different points in time and thus the behavior of the tungsten wire was different.

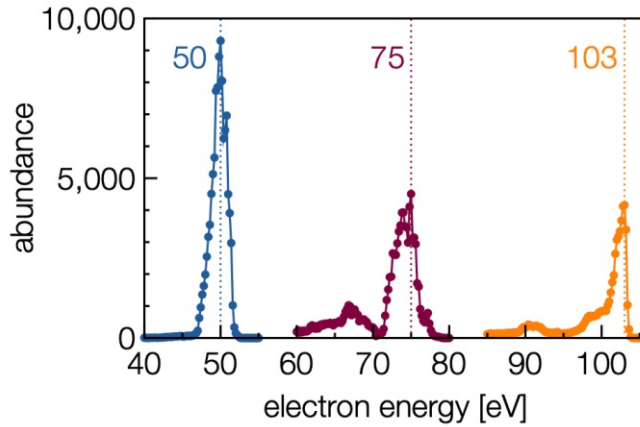


**Figure 27:** Measured electron spectra at 190 eV pass energy, 0.2 kV HVA range, 1.5 kV multiplier voltage, 270 conversion voltage, and a tungsten wire bias  $V_{\text{bias}} \in \{-50 \text{ V}, -75 \text{ V}, -100 \text{ V}\}$ . TUBUS 1 was set to ground. The measured peak positions and their corresponding electron energy are annotated in the corresponding colors.

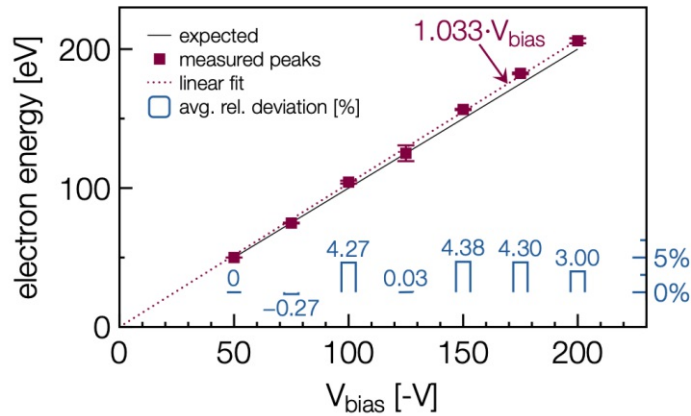


**Figure 28:** The calibration curve of the EA10+ measured during the test phase at 190 eV pass energy, a multiplier voltage ranging from 1.5 to 2.4 kV and the conversion voltage set to either the highest possible value or 390, whichever was lower. TUBUS 1 was set to ground. The measured positions of the electron peaks are plotted over the negative tungsten wire bias  $V_{\text{bias}}$ . A linear fit through these results turns out at  $1.033 \cdot V_{\text{bias}}$ , which fits the expected values of  $1.0 \cdot V_{\text{bias}}$  well. The average relative deviation from the expected value is shown in blue for all measurements underneath each respective bias voltage.

to nearly zero immediately above it. At sweep voltages corresponding to higher electron energies, no signals were measured apart from the vanishingly low noise caused by dark counts. Varying numbers of secondary electrons with lower energies are also detected.

The results of the test phase measurements were also used to calibrate the EA10+. A plot of the measured primary electron peak vs. the expected electron energy is shown in Figure 28. It was concluded that there is an offset of less than 5% from the expected value throughout the whole measured range of electron energies. This conclusion was supported by including the results from additional, individual measurements of 100 and 200 eV electrons at 2.0 kV HVA range. Due to the changed

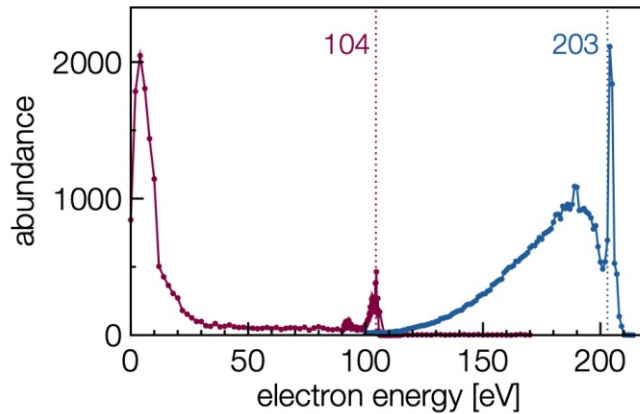


**Figure 29:** Measured electron spectra at 190 eV pass energy, 2.0 kV HVA range, 2.4 kV multiplier voltage, 390 conversion voltage, and a tungsten wire bias  $V_{\text{bias}} \in \{-100 \text{ V}, -200 \text{ V}\}$ . TUBUS 1 was set to ground during these measurements. The measured peak positions and their corresponding electron energy are annotated in the corresponding colors.

HVA range, the two electron peaks were expected—and indeed measured—at sweep voltages 0.05 and 0.1 V, respectively (see Figure 29). In general, many electrons with energies just below the maximum were detected during most measurements. Also, there were many low-energy electrons with energies just above zero up to about 20 eV. Both of these are assumed to be secondary electrons which originated from collisions of the primary ones with surrounding objects.

As described in Section 2.1, a higher pass energy results in an increased signal intensity and broader peaks. All the measurements during the test phase were conducted with 190 eV pass energy and it was noticed that the electron peaks were already relatively narrow. Measuring electron spectra with 0.01 or 0.05 V voltage step sizes ( $\equiv 0.2$  or 1 eV electron energy change), a peak is only comprised of about 3 or 7 measurement points, respectively. Consequently, reducing the pass energy for the sake of measuring spectra with an increased resolution (i.e. narrower peaks) did not seem advantageous for the test phase and the used voltage step sizes.

The results of the conducted measurements during the test phase showed that the HEA works as intended and that the peaks show up at the expected sweep voltage, or at least within 5%. Thus the analyzer was ready for measuring electrons at the NIELS experiment.

A few tungsten wire spectra were also measured at NIELS, without using the  $\mu$ -metal shield. Figure 30 shows these electron spectra with their energies defined again by an applied, negative bias. Applying no bias leads to a peak at 4 eV. Electrons with lower energies might not reach the analyzer because of magnetic stray fields or due to a decreasing analyzer efficiency. Such assumptions are supported by the fact that with an applied bias voltage, the peaks are measured approximately at the bias value and not 4 eV higher. A voltage was applied to TUBUS 1 in order to maximize the number of detected electrons. As is shown in Figure 30(b), this increases the number of detected electrons, but surprisingly also shifts the spectrum. Therefore no voltage was applied to TUBUS 1 for any other measurement presented after this point.

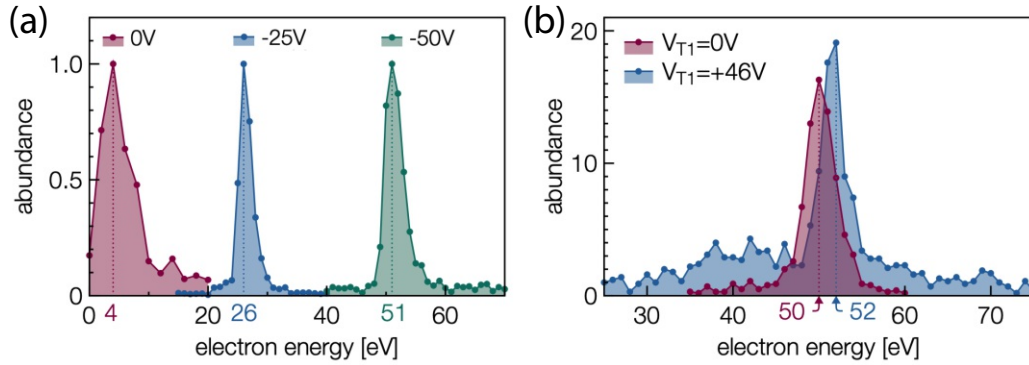


**Figure 30:** Energy spectra of electrons emitted from a tungsten wire at a current of 5 A and 7 W power input. (a) Three distinct measurements with different bias voltages  $V_{\text{bias}}$  applied to the tungsten wire and the target holder (the values are given in the legend). A voltage of  $V_{T1} = +46$  V was applied to TUBUS1 via the analyzer electronics. Each spectrum is scaled such that the maximum is 1. (b) Two measured spectra at  $V_{\text{bias}} = -50$  V with  $V_{T1} = 0$  V and  $+46$  V, respectively. The location of the maxima are labelled in the color of the corresponding plot.

### 3.2 Au (111)

For the gold irradiations, the repeller-grid in the target chamber (see Figure 20 on page 19) was set to  $-20$  V. Applying such a voltage was necessary because electrons from the ion pump caused a background signal with a peak of around 200 Hz at 3 eV. Shutting off the ion pump confirmed the suspicion that it was the source of those electrons, which reduced to nearly zero as a result. During the tungsten wire measurements, these electrons could not reach the HEA since the target holder shielded the analyzer opening. Now, the applied repeller-grid voltage reduced the number of electrons from the ion pump by more than a factor of 10, while not affecting the ion beam at all.

The described measurement series involved the Au (111) sample TUW100. It was irradiated with differently charged Xe ions and at varying angles of incidence. Figure 31 shows the results of the charge-dependent measurements at  $35^\circ$  angle of incidence. The difference in abundances does not indicate different electron yields, but it only reflects the decreasing ion current at increasing charge state (the data was not normalized). The mean values of Moyal functions fitted to the spectra all lie within  $6.83 \pm 0.27$  eV. Thus, no charge dependence of the electron energy spectra is present, given the resolution and detection efficiency of the EA10+ analyzer.

The angle-dependent spectra of irradiations with 190 keV  $\text{Xe}^{20+}$  ions can be seen in Figure 32, together with the angular dependence of the electron yield inferred from the data. The fluence of the incident ions was the same for all measurements, thus the counts can be directly compared to each other. The results reveal an increased electron yield at higher angles of incidence, i.e. when the sample is turned more toward the HEA. Fit functions  $\sim 1/\sqrt{\cos(\alpha)}$  describe the found angle-dependence well, which is in agreement with existing research [43].

It has to be noted that the referenced publication used an extraction grid in order to detect all emitted electrons, independent of the angle of incidence. The setup at the NIELS experiment did not use such a grid. Interestingly, the proposed angle dependence still fits the data well (R-squared  $> 0.97$ ). Without an extraction

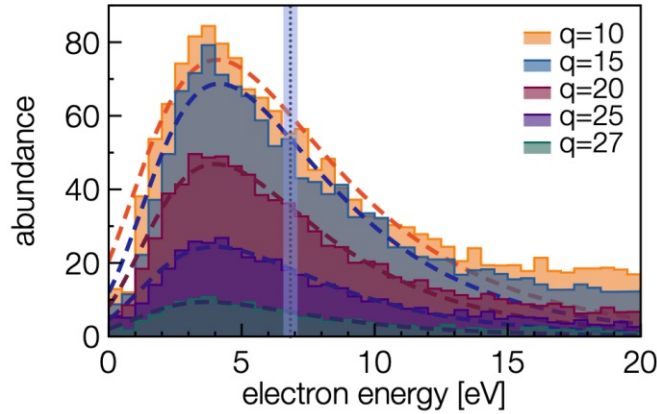


**Figure 31:** The charge-dependent electron energy spectra of the Au (111) sample irradiated with  $9.6 \cdot q$  keV  $\text{Xe}^{q+}$  ions ( $q \in \{10, 15, 20, 25, 27\}$ ) at  $\alpha = 35^\circ$ . The spectra have been fitted with Moyal functions, which are also plotted. The dotted line indicates the mean of the individual Moyal means, the light blue area is one standard deviation.

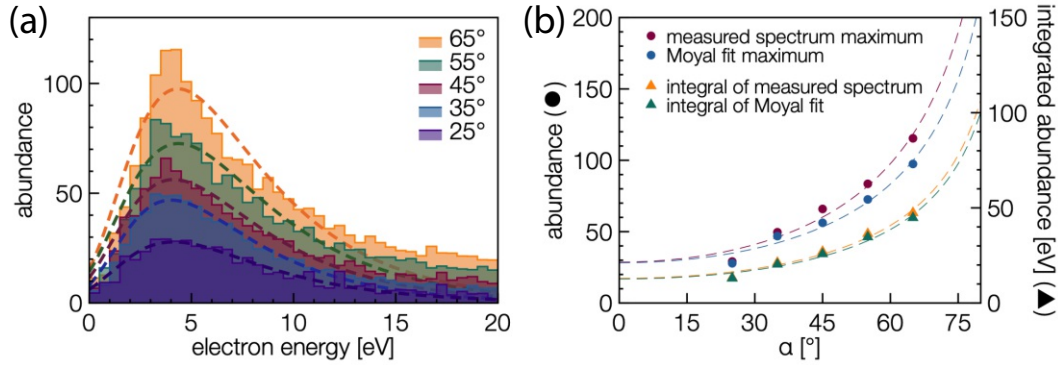


**Figure 32:** (a) Measured electron spectra during the irradiation of the Au (111) sample with 190 keV  $\text{Xe}^{20+}$  ions at angle of incidence  $\alpha \in \{25^\circ, 35^\circ, 45^\circ, 55^\circ, 65^\circ\}$ . (b) The angle dependence of both the measured and the Moyal fit maxima, as well as the integral of each of the two datasets. Fits of the form  $A + \frac{B}{\sqrt{\cos(\alpha)}}$  are also shown in (b). For the definition of  $\alpha$ , see Figure 20.

grid, the emission profile of the electrons would also have to be considered, and a decreased detection efficiency at lower angles of incidence are expected. Indeed, the measured values are consistently lower than the fit functions in Figure 32(b) predict. Thus, it is logical to assume an additional dependence on the angle between the hemispherical analyzer opening and the surface normal of the sample.

After these measurements, the  $\mu$ -metal shield was mounted to the HEA inside the target chamber and a freestanding single-layer graphene sample was added to the target holder. The  $\mu$ -metal shield prevented the ion pump electrons from reaching the analyzer, thus it was no longer necessary to apply a negative voltage to the repeller-grid. Again, electron spectra of the gold sample were measured, but no difference was found compared to the spectra gathered without the  $\mu$ -metal. One possible explanation is that the  $\mu$ -metal shield is not closed enough, thus allowing magnetic fields to reach inside. However, making the openings smaller and thereby also limiting the manipulator movement even more is not practical. Another possible issue are

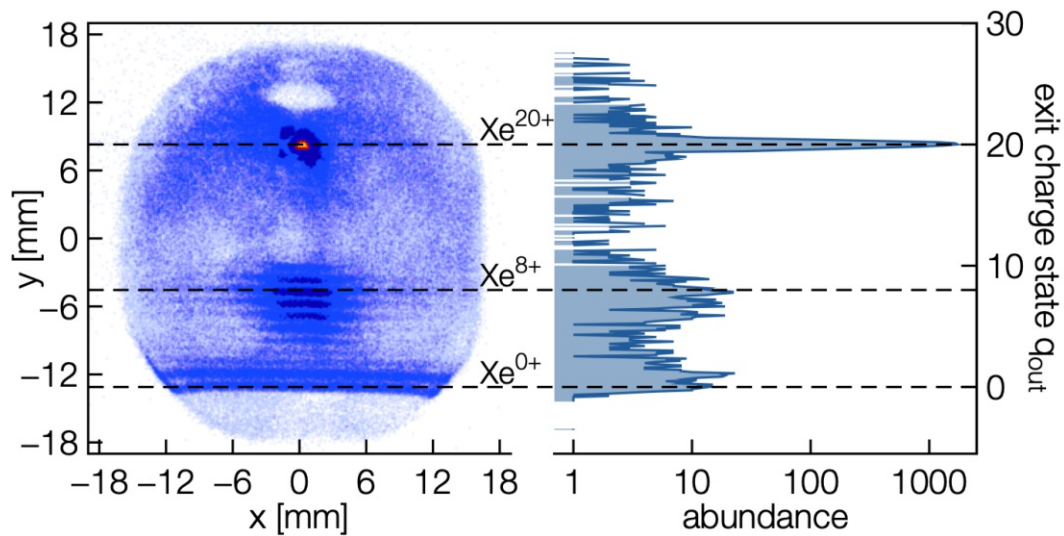


**Figure 33:** Spectrum of Xe ions on the MCP detector, which started as 190 keV  $\text{Xe}^{20+}$  and passed through heat cleaned single-layer graphene at  $30^\circ$  angle of incidence. The TOF-filtered projection of the spectrum onto the y-axis is also shown, including indicators for noteworthy exit charge states. Neutrals and singly charged ions below  $-10$  mm stem from interactions with the Quantifoil. Intermediate exit charged states interacted with the graphene and span from  $-9$  to  $-1$  mm. The  $\text{Xe}^{20+}$  ions, which did not interact with anything, are located at  $+8$  mm.

the remaining steel parts inside the  $\mu$ -metal, for example the target holder and the screws. Their remanence might be high enough such that low-energy electrons do not reach the analyzer. According to measurements with a Hall probe, the target holder has a remanence of around  $30 \mu\text{T}$  in close proximity.

### 3.3 Single-layer graphene

Measurements of ion-induced electron emission of a freestanding single-layer graphene (SLG) sample (TUW172) were all carried out at  $30^\circ$  angle of incidence using the following incident ions: 100 keV  $\text{Xe}^{20+}$ , 190 keV  $\text{Xe}^{20+}$ , and 285 keV  $\text{Xe}^{30+}$ . For these measurements, the  $\mu$ -metal shield was mounted around the target holder inside the target chamber. The Q-Blanker was set to 500 V (for 100 keV  $\text{Xe}^{20+}$ ) or 1 kV (otherwise) in order to vertically separate the transmitted ions by their exit charge state. Before heating the sample, only fully neutralized Xe,  $\text{Xe}^{1+}$ , and  $\text{Xe}^{20+}$  were visible at the micro-channel plate (MCP) detector. Then, a current of 6 A was passed for at least 30 minutes through the heating wire of the target holder, corresponding to around  $400^\circ\text{C}$ . Its effect was immediately visible after the heating procedure, since intermediate exit charge states appeared on the MCP (see Figure 33). The position of each exit charge state is interpolated from the positions of the neutral and the  $\text{Xe}^{20+}$  peak as well as their relative distance. It can be seen that ion scattering angles of SLG are much smaller (up to  $|x| < 6$  mm) than the ones of Quantifoil, whose whole scattering angle range does not fit onto the MCP width. The small scattering angles of SLG result from the fact the ions scatter only once [13]. Ions hitting the amorphous Quantifoil are scattered multiple times and thus deflected onto a broader angle interval.

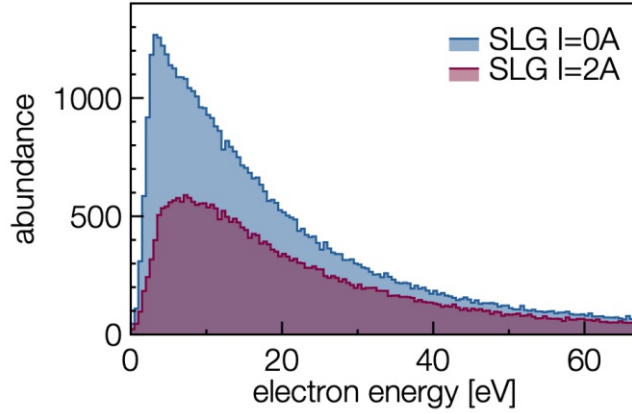


**Figure 34:** Electron spectra emitted from heat cleaned single-layer graphene during 30° 190 keV  $\text{Xe}^{20+}$  irradiation with and without a heating current of 2 A. The magnetic field resulting from the current prevents a significant portion of the low-energy electrons from reaching the detector.

Usually the heating wire current is kept at around 2 A ( $\approx 150^\circ\text{C}$ ) during measurements of freestanding 2D materials to prevent recontamination of the sample. This turned out to be infeasible for measuring low-energy electrons, since according to the Maxwell equation

$$\oint_C \mathbf{B} \cdot d\mathbf{l} = \mu_0 I$$

an enclosed, constant current  $I$  through a straight wire produces a cylindrically symmetric magnetic field

$$B(r) = \frac{\mu_0 I}{\tau r}$$

with  $\tau \equiv 2\pi$ , the vacuum permeability  $\mu_0$ , and the radial distance  $r$  from the wire. This equates to  $\approx 100 \mu\text{T}$  at the sample position. Such a field significantly reduces the number of detected low-energy electrons, as the comparison of two measurements verified (see Figure 34). Note that the spectra were not measured in coincidence with the ions and thus contain electrons with various origins, for example the gold TEM grid and the Quantifoil support. Due to the drastic reduction in detected electrons with an active heating current, the sample could only be heat-cleaned in between measurements.

The coincidence spectra of electrons emitted from SLG during the irradiation with 100 keV  $\text{Xe}^{20+}$ , 190 keV  $\text{Xe}^{20+}$ , and 285 keV  $\text{Xe}^{30+}$  ions at 30° is shown in Figure 35. To extract these electrons, the appropriate time-of-flight- (TOF) and position-filters were applied to the ions which were detected on the MCP. Thus, the number of electrons measured in coincidence with ions which interacted with SLG was obtained. The figure also includes the spectra of the electrons emitted from Quantifoil during these irradiations. In order to separate the two electron origins, the filter for the vertical position (y-axis) was tailored to the area of the corresponding ions on the MCP detector. Since the scattering angles of the ions which transmit through SLG are smaller than the MCP width (see Figure 33), the position filter for those ions also constrained events along the x-axis.

The spectra are normalized by the measurement duration and the flux of the primary ion beam, and can thus be compared directly. The electron yield of 285 keV

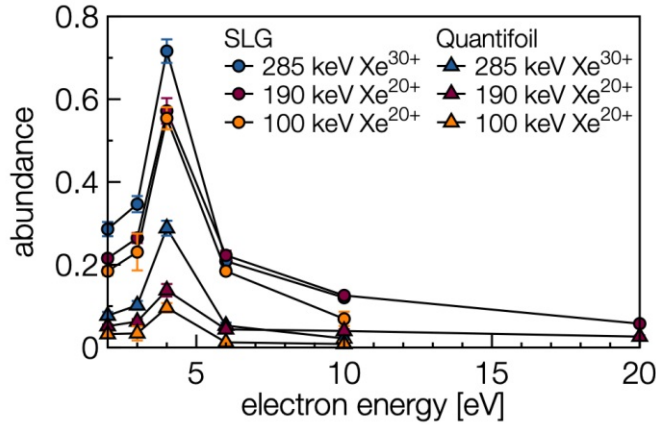


**Figure 35:** The energy spectra of primary electrons emitted from single-layer graphene and its Quantifoil support, respectively, under  $30^\circ$  irradiation with highly charged Xe ions. The individual kinetic energy and charge states are given in the legend.

$\text{Xe}^{30+}$  ions is about 1.3 times higher than the yield of  $\text{Xe}^{20+}$  ions which is in accordance with previous electron statistics experiments [22]. The yield of  $\text{Xe}^{20+}$  ions seems to be approximately the same, independent of their kinetic energy. An open question concerns the number of detected low-energy electrons. A high number might be emitted, but residual magnetic fields deflect the majority of them and they are not detected. Another possibility is that the detection efficiency of the hemispherical analyzer is not constant toward zero. These points will be investigated and hopefully solved in future experiments.

During the last series of measurements with 100 keV  $\text{Xe}^{20+}$  ions, a significant deterioration of the sample was observed through its MCP spectrum. As shown in Figure 36, the neutral and the intermediate exit charge state abundances are smaller compared to previous measurements. A reduced amount of neutral and intermediate exit charge states suggests that fewer interactions of  $\text{Xe}^{20+}$  ions with SLG occurred, i.e. that the graphene deteriorated in some form. Consistently, at the same time it was observed that fewer electrons were emitted and thus detected in coincidence with the ions. Such a deterioration of single-graphene is unexpected, since previous irradiations with 168 keV  $\text{Xe}^{38+}$  ions showed that single-layer graphene is left intact [44]. Additionally, deterioration worsened mostly between the two 100 keV  $\text{Xe}^{20+}$  irradiations, where neither the kinetic nor the potential energy should suffice to damage the sample. A possible explanation could be the fluence being much higher than  $1 \times 10^8$  ions/cm<sup>2</sup>, as it was for the measurements in the referenced publication.

Figure 37 shows an example for a measured TOF spectrum during a  $\text{Xe}^{20+}$  irradiation. The TOF is negative since it is the difference between the stop and the start signal, and the trigger (the TOF start signal) is set to the ion signal from the MCP, but the electrons reach their detector first. It can be seen that a single peak emerges from the background noise, which is otherwise comprised of random coincidences. A Gaussian is fit to the TOF peak in order to determine its position and FWHM. The evaluation of all TOF spectra revealed that both the position and the FWHM of the SLG electron TOF peak decrease with increasing electron energy, as shown in Figure 38. Electrons with higher velocity reach the detector even earlier than the

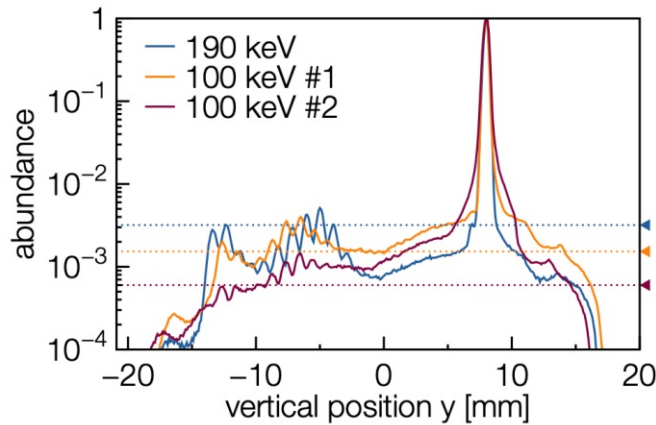


**Figure 36:** Three MCP spectra projected onto the  $y$ -axis (e.g. see Figure 33), taken from different irradiations with  $\text{Xe}^{20+}$  ions under  $30^\circ$  angle of incidence. The two 100 keV spectra were acquired a few hours apart, during which the sample was irradiated. The 190 keV spectrum was acquired multiple days prior.  $\text{Xe}^{20+}$  ion peaks are all scaled to 1 to allow direct comparison, and they are offset to the same  $y$ -position to aid the visual analysis. Neutral Xe ion peak abundances are indicated by horizontal lines, revealing their drastic decrease (note the logarithmic scale). The distribution of the intermediate exit charge states do not line up because they are different for the two used ion energies.

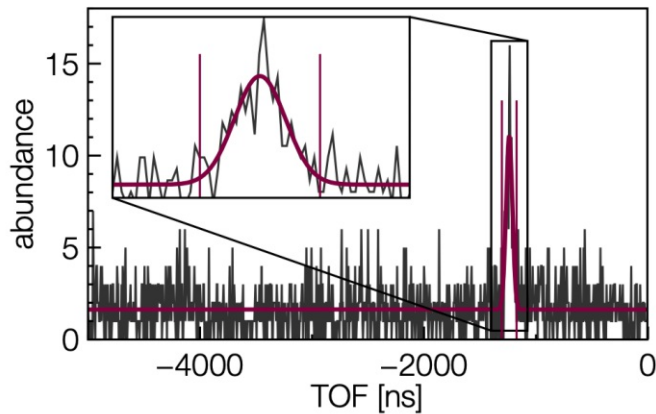


**Figure 37:** The TOF spectrum acquired during a 190 keV  $\text{Xe}^{20+}$  irradiation of single-layer graphene at  $30^\circ$  angle of incidence while measuring 4 eV electrons. Two vertical lines indicate the interval  $\mu \pm \text{FWHM}$  around the mean  $\mu$  of the Gaussian fit.

ions, thus the TOF decreases monotonically, and a  $1/v$  dependence describes the TOF peak positions well. The increasing FWHM toward low-energy electrons might be because of magnetic fields broadening the time it takes the electrons to reach the detector due to a cyclotron motion around the magnetic field lines. This additional dependence also explains why fit functions  $\sim 1/v$  (not shown) do not describe the behavior of the FWHM well.

The TOF of the ions from the target to the MCP detector can be calculated from the distance (1.164 m) and the energy of the ions, neglecting their energy loss in SLG. Using the calculated ion TOF and the measured TOF difference (i.e. peak position, see Figure 38), the electron TOF is determined and can be seen in Figure 39.

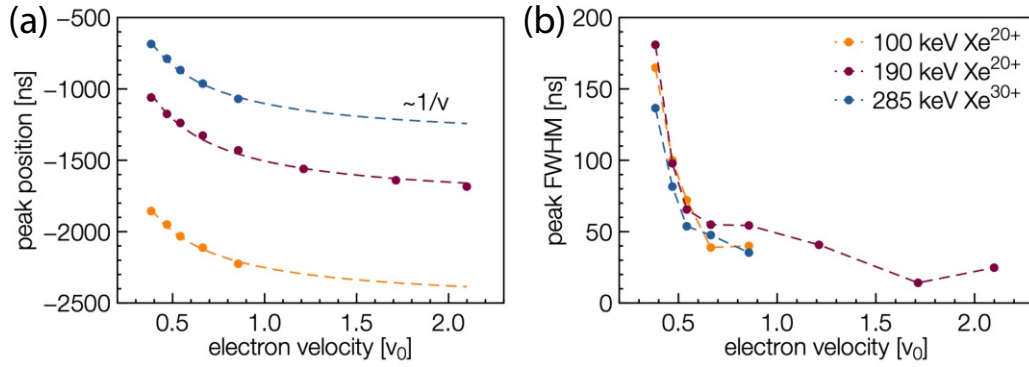


**Figure 38:** The single-layer graphene (a) TOF peak position and (b) TOF peak FWHM as functions of the electron velocity, given in units of the Bohr velocity  $v_0$ . The figure includes the data from all three ion charge states and energies used for the irradiations. Fits of the form  $A + B/v$  are also included in (a).

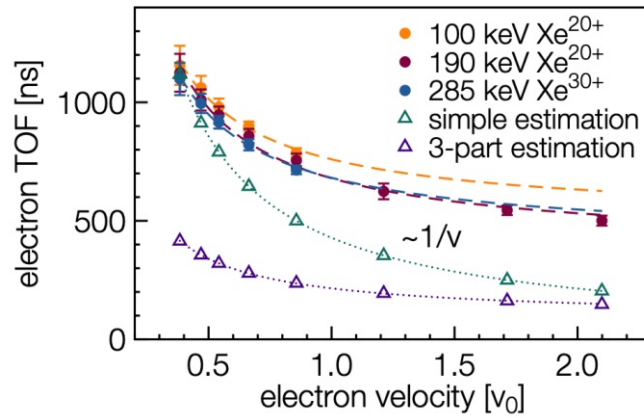


**Figure 39:** The TOF of the electrons from the sample to the detector as functions of the electron velocity, given in units of the Bohr velocity  $v_0$ . It was calculated using the ion TOF and the measured TOF difference (circular data points). The errors are the FWHM of the associated peak in the TOF spectrum. Triangle data points are the electron TOF directly estimated using their energy and the dimensions of the analyzer (see text). Fits of the form  $A + B/v$  are also shown.

The offset between the three colored curves presumably stems from the neglected ion energy loss in the single-layer graphene sample and from measurement uncertainties. The electron TOF was also estimated two different ways by using their energy and the analyzer dimensions (also shown in the figure).

The *simple estimation* (green triangles) is calculated by  $t = \frac{s}{v} = s/\sqrt{2 \cdot E_e/m_e}$ , with the electron energy  $E_e$  and its mass  $m_e$ . This model assumes a constant electron velocity  $v$  along the distance  $s$  through the energy analyzer. The distance is estimated from the analyzer dimensions given in the manual. This is only a rough approximation since the electrons are deflected and accelerated to the pass energy inside the lens system, which is not taken into account here. Consequently, it can be seen that for decreasing electron velocities, the TOF is increasingly overestimated.

The *3-part estimation* (purple triangles) extends the simple one by dividing the trajectory into three parts: Up until the center of the lens system, the electrons possess their initial energy, then they are linearly accelerated to the pass energy

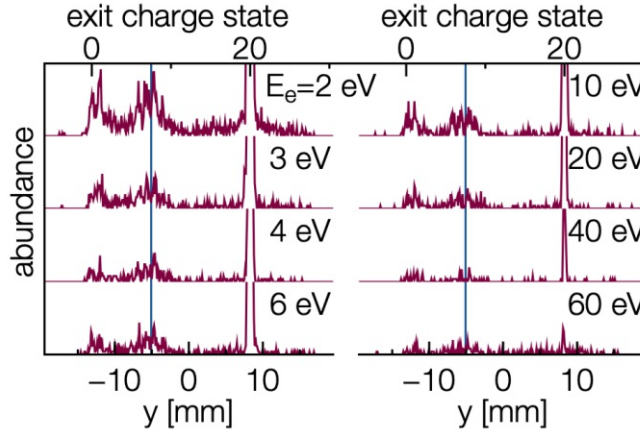


**Figure 40:** The TOF-filtered MCP spectrum projected onto the  $y$ -axis and rotated by  $90^\circ$ , given for each measured electron energy during the 190 keV  $\text{Xe}^{20+}$  irradiation of single-layer graphene at  $30^\circ$  angle of incidence. The blue lines indicate the average exit charge state ( $q_{\text{out}} = 8$ ) of the Xe ions after passing through the sample. The upper axis displays the corresponding exit charge states.

$E_{\text{pass}} = 190 \text{ eV}$  until the end of the lens system. Lastly, they traverse the remaining distance to the detector with a uniform energy  $E_e = E_{\text{pass}}$ . As a result, the electron TOF is calculated by

$$t = \frac{(0.245 \text{ m} + 0.023 \text{ m})}{\sqrt{2 \cdot E_e/m_e}} + \frac{0.263 \text{ m}}{\sqrt{(190 \text{ eV} + E_e)/m_e}} + \frac{(\pi \times 0.097 \text{ m} + 0.101 \text{ m})}{\sqrt{2 \cdot 190 \text{ eV}/m_e}}.$$

See Figure 48 in Appendix A for the dimensions of the analyzer. This estimation results in a velocity dependence which seems to better fit the curves calculated from the measured TOF difference. Still, both estimations show a significant offset from the calculated electron TOFs, maybe because additional contributions to the electron TOF were missed, or the proposed estimations are not good enough approximations.

Figure 40 shows the TOF-filtered projections of the 2D MCP spectra (cf. Figure 33) for all measured electron energies during the 190 keV  $\text{Xe}^{20+}$  irradiations. Both the ions interacting with Quantifoil as well as the ones interacting with SLG are visible since their TOF difference at this kinetic energy is too little. Furthermore, many of the  $\text{Xe}^{20+}$  ions are also part of this TOF filter due to randomly occurring coincidences.

A Gaussian fit to the intermediate exit charge states of each projected spectrum revealed the average exit charge state of the ions, which turned out to be constant ( $q_{\text{out}} = 8$ ) for all measured electron energies. Synonymously, the exit charge state distribution of the ions has an identical shape, no matter which electron energy is analyzed. This means that the electrons with different energies are all caused by the same proportion of ions within this distribution. In other words, ions with different exit charge states do not preferably cause emitted electrons with certain energies.

An analysis of the projected MCP spectra for all used ion charge states and kinetic energies revealed that the average exit charge state  $q_{\text{out}}$  for 190 keV  $\text{Xe}^{20+}$  and 285 keV  $\text{Xe}^{30+}$  ions is 8 and 18, respectively. This means that the average number of captured electrons is 12 for both of them. 100 keV  $\text{Xe}^{20+}$  ions end up in exit charge state  $q_{\text{out}} = 5$  on average, having captured around 15 electrons. All these results are in accordance with previously measured average exit charge states [36].

### 3.4 Discussion

To summarize the SLG measurements, the energy distribution of the emitted electrons under highly charged ion irradiation were successfully measured in coincidence with the transmitted ions. Since a 2D sample was investigated, secondary electron processes can be neglected and it can be assumed that the energies of *primary* electrons were measured.

Similar to the gold measurements, the energy distribution of the electrons emitted from SLG seems to be independent of the kinetic and potential ion energy. This result has to be treated with caution due to the limited amount of acquired data. Firstly, only two different kinetic energies were investigated for  $\text{Xe}^{20+}$  ions. Secondly, only two different charge states ( $\text{Xe}^{20+}$  and  $\text{Xe}^{30+}$ ) were used to check for a dependence on the potential energy. Lastly, only a limited number of measurements were carried out at selected electron energies.

The energy distribution of Quantifoil is very similar in shape to the one of SLG, which might be a systematic error. Since the SLG also covers the Quantifoil, ions which interacted with the Quantifoil might have caused electron emission from SLG. Due to the low charge state of the ions after transmission, they are classified as ones which interacted with Quantifoil. Consequently, the corresponding emitted electrons are also classified as Quantifoil electrons, although their true origin was SLG. This would explain why the Quantifoil electron energy distribution is similar to the one of SLG, and it has to be considered when filtering Quantifoil electrons.

The kinetic energy of the projectile ion influences the interaction duration with the sample. Lower kinetic energy corresponds to a longer interaction duration, more captured electrons, and thus more electrons emitted through ICD. The resulting electron yield dependence on the kinetic energy of the impinging ions is not strong, still clearly detectable [37]. The presented energy distributions did not confirm this behavior because the resolution and detection efficiency of the energy analyzer are not suited for such measurements.

In general, it is assumed that kinetic electron emission cannot be measured with the current setup when irradiating 2D materials. Due to conservation of momentum, transferred momentum from an ion to an electron also points in the direction of the ion trajectory and not toward the energy analyzer. Furthermore, no collision cascades can form inside a 2D material as they would in thicker ones, which can cause the redirection of momentum.

When a highly charged ion approaches the surface of a solid, higher charge states favor resonant transfers into higher shells of the ion [24]. Furthermore, the higher charge state implies an increased number of intermediate or inner shell vacancies. Depending on the ICD channels of the resonantly captured electrons, the created virtual photons should, on average, possess more energy compared to lower incident charge states. Consequently, the energy distribution of potential electron emission should shift or broaden toward higher energies with increasing potential energy. Since only a few electron energies were measured in this thesis, the increase might not be noticeable or resolvable. Upcoming measurements will sample the energy distribution more densely and investigate possible energy dependencies further.

Furthermore, even if de-excitation channels with higher energy differences are available for higher charge states, their corresponding rates might be negligibly small compared to the ones resulting in electron energies below 10 eV. Consequently, the

small proportion of electrons which do possess higher energies would be unable to visually change the spectrum.

For the conducted measurements, one side of the target holder was turned toward the energy analyzer by  $30^\circ$ . Thus, electrons which are emitted toward this side of the target holder are detected, the ones toward the opposite one are not. If the potential emission of electrons is symmetric around the plane of the sample, this should not cause issues. Otherwise, such an asymmetric emission profile might have to be taken into account.

There are still open questions to be answered, for example the possible inability to measure low-energy electrons and why the peak abundance is located at 4 eV. Maybe electrons with even lower energies are emitted in much higher abundances but magnetic fields prevent them from reaching the analyzer, or the analyzer efficiency at low energies decreases too much. The peak at 4 eV could be a result of the increasing electron yield convoluted with the decreasing electron detection at lower energies. Furthermore, a possible dependence of the energy distribution on the kinetic or potential ion energy might not be visible in the presented data since it is hidden in the missing low-energy electrons.

Another approach to answer questions such as the emission profile or the number of emitted electrons, and to aid the experimental work in general, is to describe the measured processes theoretically. As an example this can be done in the form of time-dependent density functional theory simulations.

## 4 TDDFT simulation

### 4.1 General description

Toma Susi at the University of Vienna applied a time-dependent density functional theory (TDDFT) model combined with Ehrenfest dynamics, which allows calculating the electron density of certain atomic setups using the code *gpaw*. The analyzed simulation is the irradiation of a graphene layer with a positively charged 100 keV Xe ion. The graphene consists of a single layer of 72 carbon atoms, and the ion is ionized eight times, i.e.  $\text{Xe}^{8+}$ . The goal of the simulation analysis was to calculate how many electrons of the graphene are captured by the ion and how many are fully emitted due to the bombardment.

The simulation divides the whole collision process into 800 equidistant time steps and the simulated space is discretized into  $256 \times 256 \times 512$  voxels. In general, voxels describe values on a regular grid in 3D space, in this case the local electron density. The individual voxel positions depend on the chosen basis vectors, which are defined as

$$\hat{e}_x = \begin{pmatrix} 0.109278 \\ 0.0 \\ 0.0 \end{pmatrix}, \hat{e}_y = \begin{pmatrix} -0.054639 \\ 0.094638 \\ 0.0 \end{pmatrix}, \hat{e}_z = \begin{pmatrix} 0.0 \\ 0.0 \\ 0.088581 \end{pmatrix}$$

in this simulation. As a result, the volume of the simulation space has the shape of a parallelepiped. The coordinates are given in units of Bohr radii  $a_0$ , with  $1 a_0 = 0.5291 \text{ \AA}$ . Figure 41 indicates the atom positions at step 140, because it shows only voxels with high electron density, which are therefore centered around the corresponding atom centers. The role of the visible orange plane is explained in the figure caption.

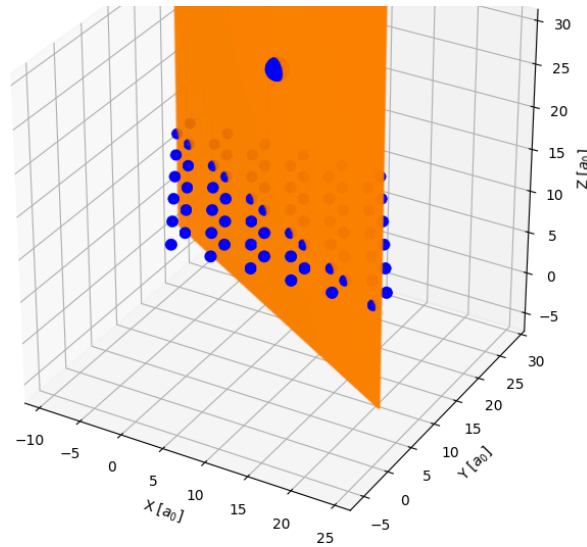


**Figure 41:** A view of the simulation space at step 140, where voxels with electron densities within  $[0.5, 1]$  electrons/ $a_0^3$  are drawn in blue. The orange plane, which bisects both the ion and a set of carbon atoms, is the one used for the 2D plots presented in this section. Starting at indices  $(i_x, i_y) = (14, 220)$  of the electron density data (or the position of the 11th carbon atom), the plane is created by incrementing  $i_x$  and decrementing  $i_y$  in an alternating fashion until  $i_y = 0$ .

The graphene layer lies in the x-y-plane at  $z \approx 11.34 a_0$ . The ion travels along a channeling trajectory in the negative z-direction, starting around  $z \approx 35.34 a_0$ , or  $24 a_0$  above the graphene layer. At the end of the simulation the ion is located at  $z \approx 5.04 a_0$ , which is  $6.3 a_0$  below the graphene.

At each step of the simulation, the TDDFT algorithm calculates the electron density for each voxel in the simulated space and saves the data into a separate *Gaussian Cube* file for every 20 steps. A cube file contains all the necessary information to fully describe the given setup: the number of atoms and their coordinates, the basis vectors of the used coordinate system, and the electron density for each voxel. Furthermore, the first two lines of the file contain comments, like the description of the included data and the order of the loops which was used for writing the cube file. Knowing the order of the x-, y-, and z-coordinate loops is essential for correctly reading the voxel data from the file.

## 4.2 Results

In this analysis the cube files for step 140 and 800 were analyzed. To calculate the number of electrons which are captured or emitted during to the ion bombardment, three additional cube files were created using the TDDFT algorithm. The first one solely contains the electron density of the unperturbed graphene layer. The other two contain the electron density of an isolated Xe ion, located at the corresponding ion position for the two analyzed steps.

Integrating the electron density of the unperturbed graphene yields the expected value of 432 electrons (72 carbon atoms with 6 electrons each). The result of integrating an isolated ion file is 46 electrons, and for the entire setup it is  $432 + 46 = 478$  electrons, both as expected. As a side note, most of the voxels have values close to zero. In fact, 93.8% of all voxels are within 0 and  $0.04 \text{ electrons}/a_0^3$ , but they only account for roughly 7% of the total charge.

By subtracting the electron densities of both the unperturbed graphene and the isolated ion from the entire setup at a certain step, the net change in electron density ( $\Delta\rho$ ) is calculated. This net change describes the perturbation caused by the interaction of the ion with the graphene layer. Integrating  $\Delta\rho$  over the volume of the graphene yields the change in the number of graphene electrons due to these interactions. The integrated volume covers the whole x-y-plane, while the z-axis range depends on the analyzed step.

For step 140, the integrated volume spans from  $z = 6$  to  $z = 15 a_0$  in order to include as much of the graphene as possible. Integrating the net electron density  $\Delta\rho$  contained within this volume turns out at around  $-1.25$  electrons. The expected result would be 0, since no electrons should be missing from the graphene at this point. This discrepancy stems from the chosen integration range, which encompasses only 99.63% (or  $430.41 = 432 - 1.59$  electrons) of the graphene electrons in the entire setup, and only 99.92% (or  $431.66 = 432 - 0.34$  electrons) of the electrons of the unperturbed graphene. Thus,  $-1.59 - (-0.34) = -1.25$  electrons are omitted by the integration of  $\Delta\rho$ , and left over as the result of the subtraction procedure. This means that the actual result of integrating  $\Delta\rho$  over the described graphene volume is 0, as expected. To conclude, the presence of the ion leaves the amount of electrons in the graphene unchanged early during the simulation. The ion does indeed have a little impact on the electron configuration of the graphene layer, which can be seen

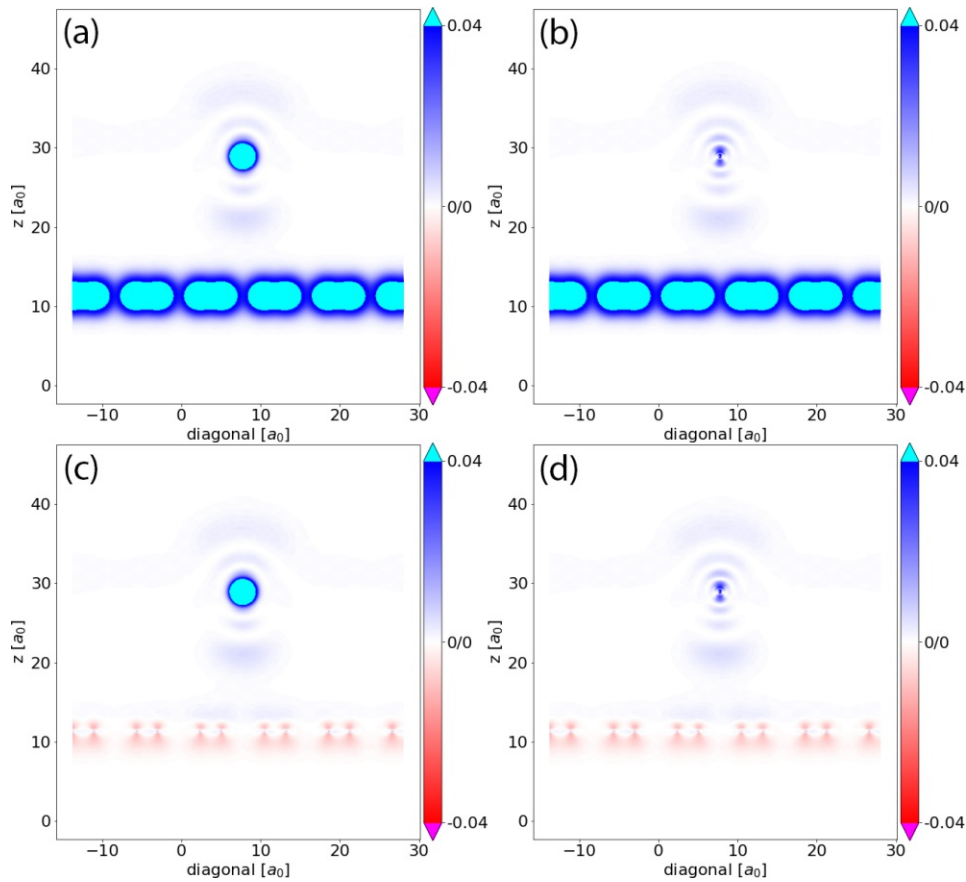


**Figure 42:** The electron density at step 140 along the plane shown in Figure 41 on page 38 for each stage of the subtraction process. (a) Nothing subtracted, (b) only the isolated ion data subtracted, (c) only the unperturbed graphene data subtracted, and (d) both the ion and the graphene data subtracted from the whole data. Absolute electron densities  $|\rho_e|$  from 0 to 0.04 electrons/ $a_0^3$  are plotted with an opacity ranging from 0 to 1. Voxels with  $\rho_e < 0$  are drawn in red (electrons missing) and the ones with  $\rho_e > 0$  in blue (electrons present). All voxels with densities outside the range are drawn in fully opaque cyan ( $\rho_e > 0.04$  electrons/ $a_0^3$ ) or magenta ( $\rho_e < -0.04$  electrons/ $a_0^3$ ).

in Figure 42. It shows the electron density at step 140 at different stages of the described subtraction process. The electron density shown in this and the upcoming figure is from a specially selected plane which bisects both the ion and a set of carbon atoms, shown in Figure 41.

For step 800, the lower bound of the  $z$ -range for integrating over the graphene is increased from 6 to  $8 a_0$ . This is necessary to avoid integrating over the electrons of the ion, which is now located at  $z \approx 5.04 a_0$ . Integrating  $\Delta\rho$  over the specified volume yields that around 9.4 electrons are missing from the graphene. The same integral over the unperturbed graphene omits 0.85 of the expected 432 electrons. Since neither the result of the integral for the entire setup nor the result of the one for  $\Delta\rho$  is known this time, the electrons omitted by the two integrals cannot be calculated. The integration result can therefore not be compensated by the amount of omitted electrons. From now on, they will be considered part of the caught or emitted electrons. The electron density at step 800 is shown in Figure 43, again at the four stages of the subtraction process. The effect of the ion on the graphene can

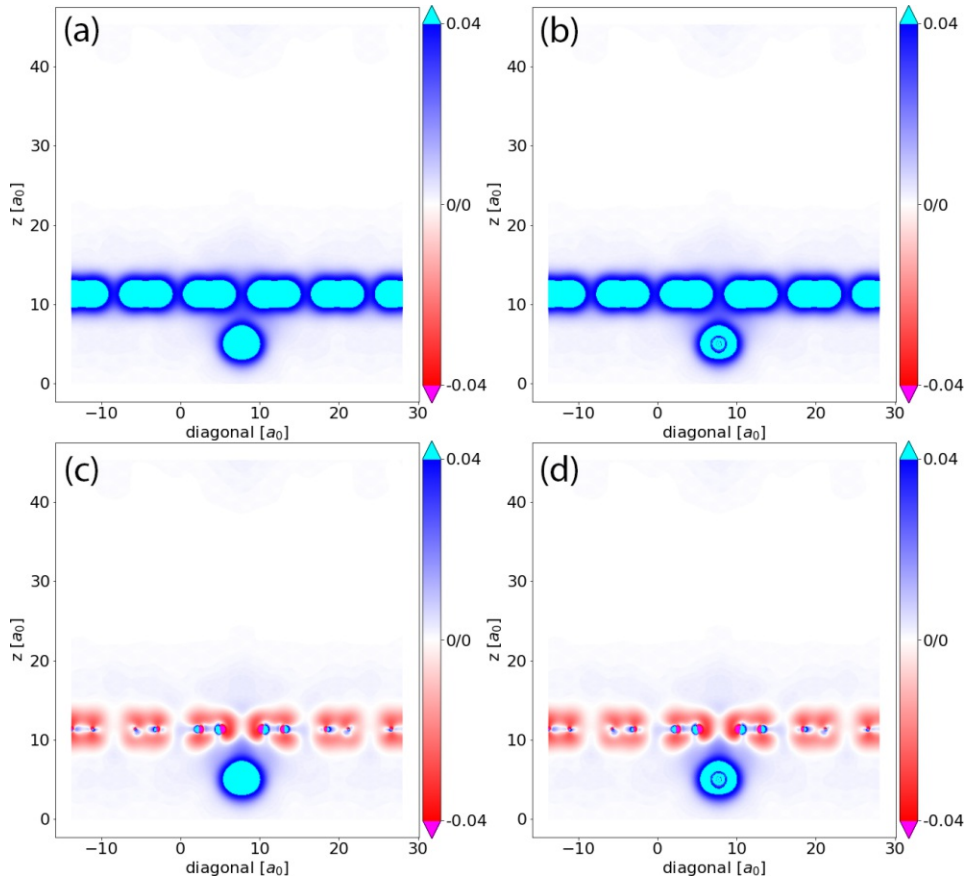


**Figure 43:** The electron density at step 800 along the plane shown in Figure 41 on page 38 for each stage of the subtraction process. (a) Nothing subtracted, (b) only the isolated ion data subtracted, (c) only the unperturbed graphene data subtracted, and (d) both the ion and the graphene data subtracted from the whole data. Absolute electron densities  $|\rho_e|$  from 0 to 0.04 electrons/ $a_0^3$  are plotted with an opacity ranging from 0 to 1. Voxels with  $\rho_e < 0$  are drawn in red (electrons missing) and the ones with  $\rho_e > 0$  in blue (electrons present). All voxels with densities outside the range are drawn in fully opaque cyan ( $\rho_e > 0.04$  electrons/ $a_0^3$ ) or magenta ( $\rho_e < -0.04$  electrons/ $a_0^3$ ).

be clearly seen by comparing it to Figure 42.

To better understand the individual contributions to the integral of  $\Delta\rho$  over the graphene volume, an integration of the whole x-y-plane was carried out for each individual z-coordinate from  $z = 0$  to  $z \approx 22.6 a_0$  in steps of  $\delta z = \hat{e}_{z,3} = 0.088581 a_0$ :

$$N_e(z) = \int_x \int_y \int_z^{z+\delta z} \Delta\rho d\mathbf{x}. \quad (2)$$

The results of these calculations for both analyzed steps are shown in Figure 44. The plot shows that for step 140 nearly all of the graphene was removed by the subtraction of the unperturbed graphene data. Only minuscule amounts remain, which are perturbations caused by the presence of the ion. For step 800 on the other hand, much more remains after the subtraction. Around the graphene layer, peaks of missing electrons can be seen, while surplus electrons remain around the ion. This result leads to the conclusion that the ion captures electrons from the graphene. However, it does not clearly show whether all electrons missing from the graphene

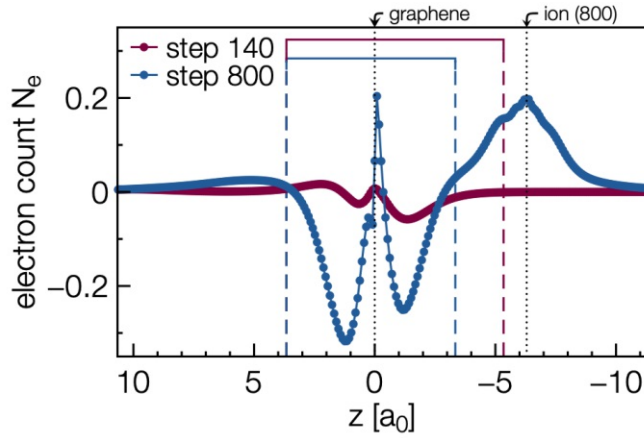


**Figure 44:** The number of electrons in each x-y-plane, calculated for both analyzed steps using Equation 2. The x-axis shows the z-position relative to the graphene layer. The brackets indicate the range used for integrating the whole graphene layer at each respective step. They reveal that integrating over the larger interval at step 800 would include not only the graphene but also some of the residual parts of the ion after the subtraction, i.e. captured electrons.

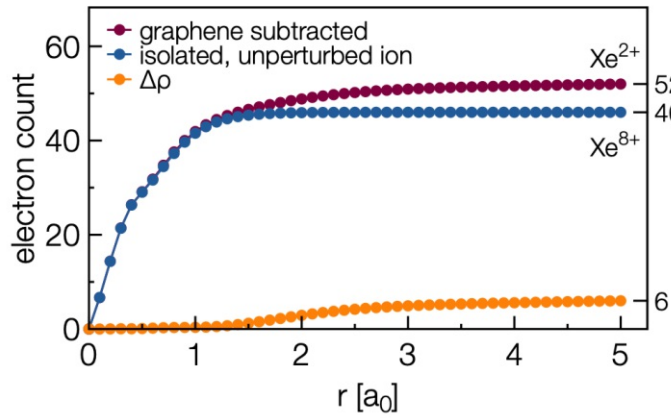


**Figure 45:** The number of electrons contained within a sphere of radius  $r \in [0.1, 5.0] a_0$ , which is located at the ion position at step 800. The integration was carried out for three cases: only the graphene subtracted (purple), the isolated ion (blue), and the net electron density  $\Delta\rho$  (orange).

have been captured by the ion. Some electrons might also have been fully emitted from the graphene during the collision process.

To find out what exactly happened to the 9.4 missing electrons determined at step 800, spherical integrations were carried out around the position of the ion for three different cube files. The integrations were performed with increasing sphere radii from  $0.1$  to  $5.0 a_0$  in steps of  $0.1 a_0$  and the results are shown in Figure 45. The plots once again confirm that integrating the ion on its own turns out at 46 electrons within a radius of  $1.5 a_0$ . Furthermore, the results also show that the ion captures 6 electrons. This conclusion is reinforced by theoretical calculations of the Xe Hirshfeld charge, which were carried out also by Toma Susi. His calculations show that the ion is in state  $\text{Xe}^{2+}$  after passing through the graphene layer, i.e. that it captured 6 electrons (see Figure 46).

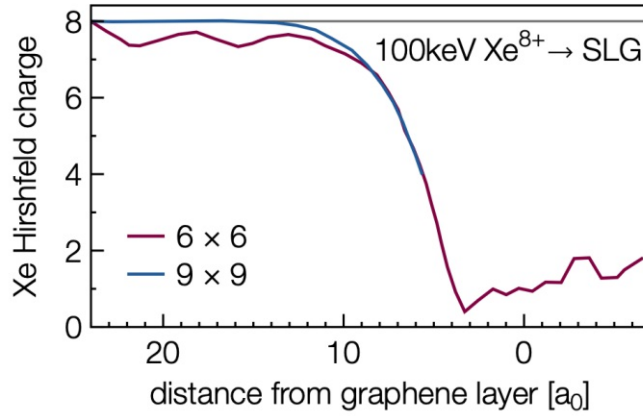


**Figure 46:** The Hirshfeld charge of the Xe ion as a function of the distance from the graphene layer in Bohr radii  $a_0$ , calculated with two different cell sizes:  $6 \times 6$  and  $9 \times 9$ . The analysis was carried out on the smaller cell size. The bigger one behaves better but it could only be run for a limited distance due to the increased computation time. The final ion charge state after passing the graphene is  $q \approx 2$ , i.e.  $\text{Xe}^{2+}$ .

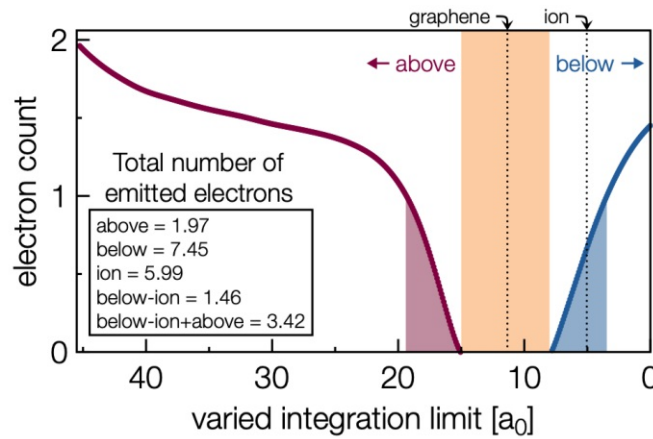


**Figure 47:** The result of integrating  $\Delta\rho$  at step 800 over the volumes above and below the graphene layer, whose extent is indicated in orange. For the integration below the graphene, a sphere with radius  $5 a_0$  around the ion position is omitted. The thereby calculated number of electrons is plotted over a varying limit of the integration. The integration above the graphene layer always starts at  $z = 15 a_0$  and ends at  $z \in [15, 45] a_0$ . Below the graphene, the integration starts at  $z \in [0, 8] a_0$  and ends at  $z = 8 a_0$ . The two filled areas below the curves each equal 1 electron.

Since the Xe ion captures 6 electrons, it is implied that the other 3.4 missing electrons are emitted from the graphene due to the interactions with the ion. Where exactly these electrons end up during the simulation was investigated by integrating the volumes which are not occupied by atoms. These volumes comprise everything above ( $z \geq 15 a_0$ ) and below ( $z \leq 8 a_0$ ) the graphene layer, while also excluding the voxels within a radius of  $5 a_0$  around the Xe ion. The results are shown in Figure 47. They imply that around 2 electrons are still located close to the ion and the graphene layer. The remaining charges are distributed over a wide range above and below the graphene layer. They all sum up to the before calculated value of around 3.4 electrons. To solely determine the total number of emitted electrons,

both volumes above and below the graphene layer are integrated and the number of captured electrons is simply subtracted, which then yields the same result of about 3.4 electrons (see inset text in the figure). This approach to calculate the total number of emitted electrons was afterwards also found to be used in published research [45]. It is not expected that emitted electrons are recaptured because of the quick charge dissipation in graphene which prevents a positive charge patch (due to the missing electrons) from building up [10, 11]. The integration curves in Figure 47 show that the emission is close to symmetric around the graphene layer. This means that there is no apparent disadvantage in measuring the energy distribution of emitted electrons solely in backwards direction, as it is currently the case at the NIELS experiment.

In conclusion, the analysis was not completely unambiguous because the ion at step 800 is still relatively close to the graphene and their electron densities partly overlap. For future analyses, the simulation will be run longer to ensure that the ion is farther away from the graphene. Consequently, the electron densities of the two will be completely separated and it will be easier to integrate over each of them, thus minimizing the error caused by omitted electrons. It will also be easier to integrate over the rest of the simulation space in order to investigate the time-evolution of the missing electrons. To investigate the measurements described in this thesis using the same TDDFT approach, higher charge states would have to be simulated, which is currently not possible. On the other hand, irradiations with 100 keV  $\text{Xe}^{8+}$  ions are not possible at the NIELS experiment since the ion source can only produce  $\text{Xe}^{8+}$  ions with kinetic energies up to 80 keV. Apart from the planned improvements and known shortcomings, the current results already show that this analysis procedure provides a neat way to calculate the number of captured and emitted electrons caused by the impact of an ion.

## 5 Summary and outlook

The goal of this thesis was putting a hemispherical analyzer (HEA) in operation in order to measure the energy distribution of the ion-induced, emitted electrons of single-layer graphene (SLG) at the NIELS experiment. An initial test phase was undertaken on a specially constructed test rig. This phase included testing and calibrating the analyzer. Multiple measurements were conducted to confirm its functionality by acquiring spectra of electrons emitted from a tungsten wire.

After the test phase, the HEA was mounted to the existing structure of the NIELS experiment. A new target holder and an associated  $\mu$ -metal shielding were designed, manufactured, and also mounted. A freestanding SLG sample and a Au (111) sample were irradiated with highly charged  $\text{Xe}^{q+}$  ( $q \in [10, 30]$ ) ions, whose kinetic energy ranged from 95 to 285 keV. For SLG, the emitted electrons were measured in coincidence with the detected ions. Consequently, the energy distribution of electrons only emitted from SLG could be determined. Since SLG is a 2D material, it can be assumed that most of the emitted electrons are directly detected and do not interact with other particles. Thus, the measurements revealed the energy distribution of the *primary* electrons which are emitted during the interaction of highly charged Xe ions and SLG.

The gold measurements find an angle-dependent electron yield, which matches existing fits in literature well [43]. Results of both the gold and the SLG sample suggest that the energy distribution of the emitted electrons does not depend on the energy of the ions, neither kinetic nor potential. The electron yield of SLG increases with higher ion charge states and is higher than the one of Quantifoil, which is in accordance with results from previous experiments [22]. The majority of the electrons possess energies below 10 eV with a consistent peak at 4 eV. This result supports the prediction of Interatomic Coulombic Decay, which states that many low-energy electrons are expected from this process [38]. Questions regarding the abundance of low-energy electrons below 4 eV and their broad time-of-flight peak will be investigated in future experiments. Additionally, the measurements will be conducted with higher resolution, thus sampling the energy distribution at many more points. Possible changes in the energy distribution of emitted electrons with varying ion energy, charge state, angle of incidence, or other types of 2D materials altogether are also planned.

A new electronics setup was established at the NIELS experiment in order to enable measuring ions and electrons at their respective detectors in coincidence. The process of acquiring electron energy spectra with the HEA was fully automated through newly created software. The data evaluation and analysis was also automated via a Python script which calculates the electron count for all the measured energies with the option to apply time-of-flight- and position-filters.

Besides the experimental work, analysis of a time-dependent density functional theory simulation was conducted to investigate whether electron emission can be modeled by it. The simulation calculated the electron density during the bombardment of single-layer graphene with a 100 keV  $\text{Xe}^{8+}$  ion. Analyzing the simulation data revealed that the Xe ion captures around 6 electrons while passing through the graphene layer. This result is in accordance with the existing theoretical prediction stemming from a calculation of the ion Hirshfeld charge. Furthermore, the

conducted analysis shows that around 3 electrons are emitted from the graphene due to the interactions with the ion. Future simulations of additional time steps after the collision will be run in order to simplify the analysis procedure and allow for a deeper investigation of the time-evolution of the emitted electrons. Hopefully, simulations of higher ion charge states will be possible in the future to better represent the conducted experiments. All in all, it turned out that the described analysis procedure of the simulation data is a feasible approach for calculating the number of captured and emitted electrons for ion bombardment scenarios.

## Danksagung

Danke Fritz für dein offenes Ohr, welches du uns stets für die Herausforderungen des Laboralltags bietest. Ich weiß es sehr zu schätzen, wie du dir als viel beschäftigter Institutsvorstand immer die Zeit nimmst, dein Verständnis für die Thematik und deine langjährige Erfahrung mit uns zu teilen. Ein großes Danke ergeht an Richard für deine tolle Betreuung meiner Diplomarbeit, für deine Mithilfe im Labor und die Unmengen an Wissen, welche ich mir durch deine Erklärungen aneignen konnte. Dankeschön an meine Betreuerin Anna, für dein pausenloses Mitfiebern und die ständige Bereitschaft, sich jeder Problemstellung zu widmen und sie bestmöglich zu lösen. Danke, dass du mich Anteil haben ließest an deiner ansteckenden Begeisterung dafür, Wissen zu schaffen. Auch außerhalb der wissenschaftlichen Arbeit gebührt dir großes Lob für deinen fantastischen Einsatz in der Arbeitsgruppe. Ein sehr lautes Danke schallt Richtung Berkeley an Paul dafür, dass du mich bereits bei meiner Bachelorarbeit hervorragend betreutest und stets kluge, durchdachte Ideen sowie Humor einzubringen weist. Danke Herbert, dass ich mich immer für Rat an dich wenden konnte, und du viele individuelle Problemstellungen schnell und intelligent zu lösen wusstest. Danke an Michael Schmid aus der Arbeitsgruppe von Ulrike Diebold für das Leihen des hemisphärischen Analysators sowie die Unterstützung bei Fragen zum Gerät. Ich bedanke mich speziell bei allen KollegInnen, die bereit waren, den Manipulator samt Probenhalter zigital manuell von der Vakuumkammer herunter- und wieder hochzuheben. Ein umfassendes Dankeschön geht an alle Mitglieder der Arbeitsgruppe, durch deren Erzählungen ich viel über sie und ihre Experimente erfahren durfte, die immer für eine nette Stimmung sorgten und die mit diesem Perspektivenwechsel den oft undurchdringlichen Wald voll eigener Probleme durchaus zu lichten schafften. Abschließend ein riesiges Danke an meine Familie, dass es von eurer Seite nie an Unterstützung mangelt und ihr es mir ermöglicht habt, diesen Weg zu gehen.

## References

- [1] S. Martin, R. Brédy, J. Bernard, J. Désesquelles, and L. Chen. Very fast hollow-atom decay processes in  $\text{Xe}^{30+}$ - $\text{C}_{60}$  collisions. *Physical Review Letters*, 89:183401, 2002.
- [2] P. Ernst, R. Kozubek, L. Madauß, J. Sonntag, A. Lorke, and M. Schleberger. Irradiation of graphene field effect transistors with highly charged ions. *Nuclear Instruments and Methods in Physics Research Section B: Beam Interactions with Materials and Atoms*, 382:71, 2016.
- [3] M. Djebli, A. Kiouche, A. S. El-Said, and H. Bahlouli. On the formation of surface nanostructures induced by slow highly charged ions. *Physics of Plasmas*, 24:072115, 2017.
- [4] F. Aumayr, S. Facsko, A. S. El-Said, C. Trautmann, and M. Schleberger. Single ion induced surface nanostructures: a comparison between slow highly charged and swift heavy ions. *Journal of Physics: Condensed Matter*, 23:393001, 2011.
- [5] R. Ritter, R. A. Wilhelm, M. Stöger-Pollach, R. Heller, A. Mücklich, U. Werner, H. Vieker, A. Beyer, S. Facsko, A. Gözlhäuser, and F. Aumayr. Fabrication of nanopores in 1 nm thick carbon nanomembranes with slow highly charged ions. *Applied Physics Letters*, 102:063112, 2013.
- [6] R. A. Wilhelm, E. Gruber, R. Ritter, R. Heller, A. Beyer, A. Turchanin, N. Klingner, R. Hübner, M. Stöger-Pollach, H. Vieker, G. Hlawacek, A. Gözlhäuser, S. Facsko, and F. Aumayr. Threshold and efficiency for perforation of 1 nm thick carbon nanomembranes with slow highly charged ions. *2D Materials*, 2:035009, 2015.
- [7] J. Buchheim, R. M. Wyss, I. Shorubalko, and H. G. Park. Understanding the interaction between energetic ions and freestanding graphene towards practical 2D perforation. *Nanoscale*, 8:9, 2016.
- [8] H. Peng, M. Sun, F. Liu, D. Yang, D. Zhang, W. Yuan, X. Du, H. Chen, L. Wang, and T. Wang. Potential effect on the interaction of highly charged ion with graphene. *Nuclear Instruments and Methods in Physics Research Section B: Beam Interactions with Materials and Atoms*, 407:291, 2017.
- [9] S. Creutzburg, J. Schwestka, A. Niggas, H. Inani, M. Tripathi, A. George, R. Heller, R. Kozubek, L. Madauß, N. McEvoy, S. Facsko, J. Kotakoski, M. Schleberger, A. Turchanin, P. L. Grande, F. Aumayr, and R. A. Wilhelm. Vanishing influence of the band gap on the charge exchange of slow highly charged ions in freestanding single-layer  $\text{MoS}_2$ . *Physical Review B*, 102:045408, 2020.
- [10] R. A. Wilhelm, E. Gruber, J. Schwestka, R. Heller, S. Facsko, and F. Aumayr. Neutralization dynamics of slow highly charged ions in 2D materials. *Applied Sciences*, 8:1050, 2018.

- [11] E. Gruber, R. A. Wilhelm, R. Pétuya, V. Smejkal, R. Kozubek, A. Hierzenberger, B. C. Bayer, I. Aldazabal, A. K. Kazansky, F. Libisch, A. V. Krasheninnikov, M. Schleberger, S. Facsko, A. G. Borisov, A. Arnau, and F. Aumayr. Ultrafast electronic response of graphene to a strong and localized electric field. *Nature Communications*, 7:13948, 2016.
- [12] R. A. Wilhelm, E. Gruber, R. Ritter, R. Heller, S. Facsko, and F. Aumayr. Charge exchange and energy loss of slow highly charged ions in 1 nm thick carbon nanomembranes. *Physical Review Letters*, 112:153201, 2014.
- [13] S. Creutzburg, A. Niggas, D. Weichselbaum, P. L. Grande, F. Aumayr, and R. A. Wilhelm. Angle-dependent charge exchange and energy loss of slow highly charged ions in freestanding graphene. *Physical Review A*, 104:042806, 2021.
- [14] A. Niggas, J. Schwestka, S. Creutzburg, T. Gupta, D. Eder, B. C. Bayer, F. Aumayr, and R. A. Wilhelm. The role of contaminations in ion beam spectroscopy with freestanding 2D materials: A study on thermal treatment. *The Journal of Chemical Physics*, 153:014702, 2020.
- [15] M. Schleberger and J. Kotakoski. 2D material science: Defect engineering by particle irradiation. *Materials*, 11:1885, 2018.
- [16] Z. Li and F. Chen. Ion beam modification of two-dimensional materials: Characterization, properties, and applications. *Applied Physics Reviews*, 4:011103, 2017.
- [17] M. Ghorbani-Asl, S. Kretschmer, D. E. Spearot, and A. V. Krasheninnikov. Two-dimensional MoS<sub>2</sub> under ion irradiation: from controlled defect production to electronic structure engineering. *2D Materials*, 4:025078, 2017.
- [18] R. Kozubek, M. Tripathi, M. Ghorbani-Asl, S. Kretschmer, L. Madauß, E. Pollmann, M. O'Brien, N. McEvoy, U. Ludacka, T. Susi, G. S. Duesberg, R. A. Wilhelm, A. V. Krasheninnikov, J. Kotakoski, and M. Schleberger. Perforating freestanding molybdenum disulfide monolayers with highly charged ions. *The Journal of Physical Chemistry Letters*, 10:904, 2019.
- [19] X. Chen, Y. Liu, W. Gao, G. Yang, A. H. Qureshi, M. Chen, X. Yao, M. Zhou, X. Zhang, and Y. Liu. High electrocatalytic activity of defected MX<sub>2</sub>/graphene heterostructures (M= Mo, W; X= S, Se) for hydrogen evolution reaction. *The Journal of Physical Chemistry C*, 125:15292, 2021.
- [20] F. Aumayr, G. Lakits, and HP. Winter. On the measurement of statistics for particle-induced electron emission from a clean metal surface. *Applied Surface Science*, 47:139, 1991.
- [21] C. Lemell, J. Stöckl, HP. Winter, and F. Aumayr. A versatile electron detector for studies on ion-surface scattering. *Review of Scientific Instruments*, 70:1653, 1999.
- [22] J. Schwestka, A. Niggas, S. Creutzburg, R. Kozubek, R. Heller, M. Schleberger, R. A. Wilhelm, and F. Aumayr. Charge-exchange-driven low-energy electron

splash induced by heavy ion impact on condensed matter. *The Journal of Physical Chemistry Letters*, 10:4805, 2019.

- [23] F. Aumayr and HP. Winter. Potential sputtering. *Philosophical Transactions of the Royal Society of London. Series A: Mathematical, Physical and Engineering Sciences*, 362:77, 2004.
- [24] J. Burgdörfer, P. Lerner, and F. W. Meyer. Above-surface neutralization of highly charged ions: The classical over-the-barrier model. *Physical Review A*, 44:5674, 1991.
- [25] HP. Winter and F. Aumayr. Hollow atoms. *Journal of Physics B: Atomic, Molecular and Optical Physics*, 32:R39, 1999.
- [26] A. Arnau, F. Aumayr, P. M. Echenique, M. Grether, W. Heiland, J. Limburg, R. Morgenstern, P. Roncin, S. Schippers, R. Schuch, N. Stolterfoht, P. Varga, T. J. M. Zouros, and HP. Winter. Interaction of slow multicharged ions with solid surfaces. *Surface Science Reports*, 27:113, 1997.
- [27] D. Hasselkamp, H. Rothard, K. O. Groeneveld, J. Kemmler, P. Varga, and HP. Winter. *Particle induced electron emission II*, volume 123. 2006.
- [28] M. Hattass, T. Schenkel, A. V. Hamza, A. V. Barnes, M. W. Newman, J. W. McDonald, T. R. Niedermayr, G. A. Machicoane, and D. H. Schneider. Charge equilibration time of slow, highly charged ions in solids. *Physical Review Letters*, 82:4795, 1999.
- [29] L. S. Cederbaum, J. Zobeley, and F. Tarantelli. Giant intermolecular decay and fragmentation of clusters. *Physical Review Letters*, 79:4778, 1997.
- [30] R. A. Wilhelm, E. Gruber, J. Schwestka, R. Kozubek, T. I. Madeira, José P. Marques, J. Kobus, A. V. Krashennnikov, M. Schleberger, and F. Aumayr. Interatomic coulombic decay: The mechanism for rapid deexcitation of hollow atoms. *Physical Review Letters*, 119:103401, 2017.
- [31] J. Rist, T. Miteva, B. Gaire, H. Sann, F. Trinter, M. Keiling, N. Gehrken, A. Moradmand, B. Berry, M. Zohrabi, M. Kunitski, I. Ben-Itzhak, A. Belkacem, T. Weber, A. L. Landers, M. Schöffler, J. B. Williams, P. Kolorenč, K. Gokhberg, T. Jahnke, and R. Dörner. A comprehensive study of Interatomic Coulombic Decay in argon dimers: Extracting R-dependent absolute decay rates from the experiment. *Chemical Physics*, 482:185, 2017.
- [32] R. A. Wilhelm and P. L. Grande. Unraveling energy loss processes of low energy heavy ions in 2d materials. *Communications Physics*, 2:1, 2019.
- [33] J. F. Ziegler, M. D. Ziegler, and J. P. Biersack. SRIM - The stopping and range of ions in matter (2010). *Nuclear Instruments and Methods in Physics Research Section B: Beam Interactions with Materials and Atoms*, 268:1818, 2010.
- [34] E. Gruber. *Interaction of ions with 3D and 2D materials*. PhD thesis, TU Wien, 2017.

- [35] D. Fink and L. T. Chadderton. Ion-solid interaction: status and perspectives. *Brazilian Journal of Physics*, 35:735, 2005.
- [36] A. Niggas, S. Creutzburg, J. Schwestka, B. Wöckinger, T. Gupta, P. L. Grande, D. Eder, J. P. Marques, B. C. Bayer, F. Aumayr, R. Bennett, and R. A. Wilhelm. Peeling graphite layer by layer reveals the charge exchange dynamics of ions inside a solid. *Communications Physics*, 4:180, 2021.
- [37] A. Niggas, J. Schwestka, K. Balzer, D. Weichselbaum, R. Heller, S. Creutzburg, H. Inani, M. Tripathi, N. McEvoy, J. Kotakoski, A. George, A. Turchanin, M. Bonitz, F. Aumayr, and R. A. Wilhelm. Ion-induced surface charge dynamics in freestanding monolayers of graphene and MoS<sub>2</sub> probed by the emission of electrons. in preparation, 2021.
- [38] T. Jahnke. Interatomic and intermolecular Coulombic decay: the coming of age story. *Journal of Physics B: Atomic, Molecular and Optical Physics*, 48:082001, 2015.
- [39] J. Schwestka, A. Niggas, S. Creutzburg, R. Kozubek, L. Madauß, R. Heller, M. Schleberger, S. Facsko, R. A. Wilhelm, and F. Aumayr. Highly charged ion impact on graphene leading to the emission of low energy electrons. *Journal of Physics: Conference Series*, 1412:202012, 2020.
- [40] D. Roy and D. Tremblay. Design of electron spectrometers. *Reports on Progress in Physics*, 53:1621, 1990.
- [41] J. F. Watts and J. Wolstenholme. *An Introduction to Surface Analysis by XPS and AES*. John Wiley & Sons, 2003.
- [42] J. Schwestka, D. Melinc, R. Heller, A. Niggas, L. Leonhartsberger, H. Winter, S. Facsko, F. Aumayr, and R. A. Wilhelm. A versatile ion beam spectrometer for studies of ion interaction with 2D materials. *Review of Scientific Instruments*, 89:085101, 2018.
- [43] W. Meissl, M. C. Simon, J. R. Crespo López-Urrutia, H. Tawara, J. Ullrich, HP. Winter, and F. Aumayr. Highly charged ion-induced potential electron emission from clean Au (1 1 1): Dependence on the projectile angle of incidence. *Nuclear Instruments and Methods in Physics Research Section B: Beam Interactions with Materials and Atoms*, 256:520, 2007.
- [44] J. Schwestka, H. Inani, M. Tripathi, A. Niggas, N. McEvoy, F. Libisch, F. Aumayr, J. Kotakoski, and R. A. Wilhelm. Atomic-Scale Carving of Nanopores into a van der Waals Heterostructure with Slow Highly Charged Ions. *ACS nano*, 14:10536, 2020.
- [45] A. Kononov and A. Schleife. Anomalous stopping and charge transfer in proton-irradiated graphene. *Nano Letters*, 21:4816, 2021.

## A SolidWorks drawings

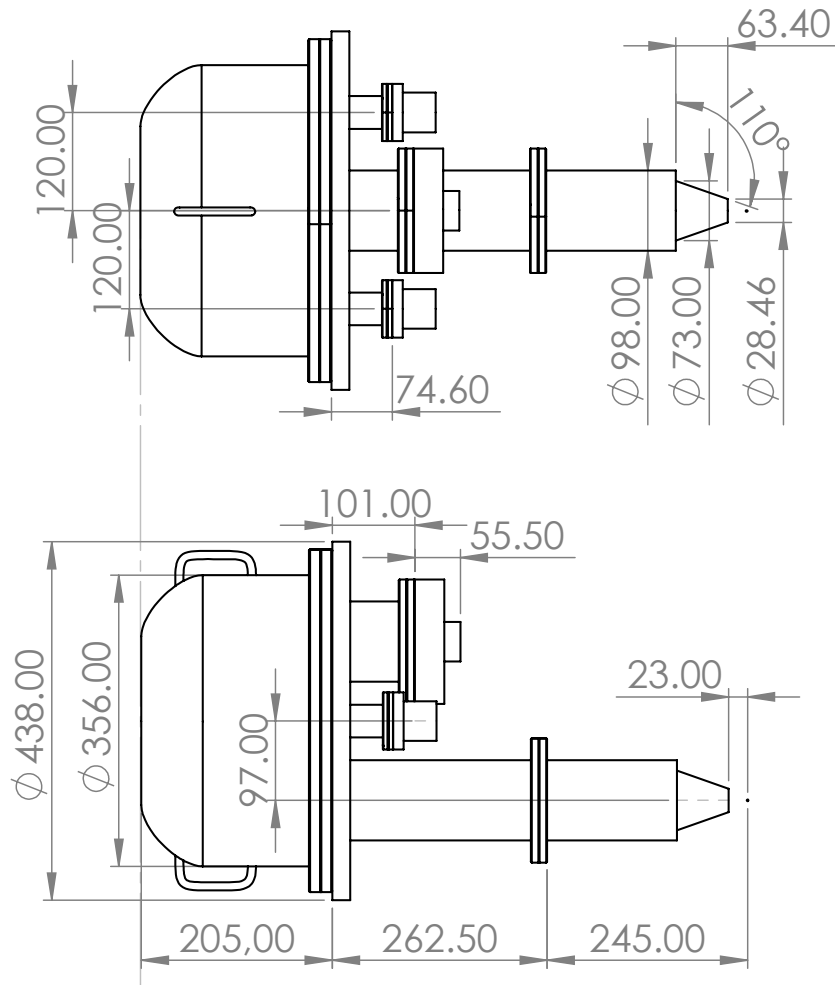


**Figure 48:** SolidWorks drawing of the hemispherical analyzer EA10+. Dimensions are given in mm.

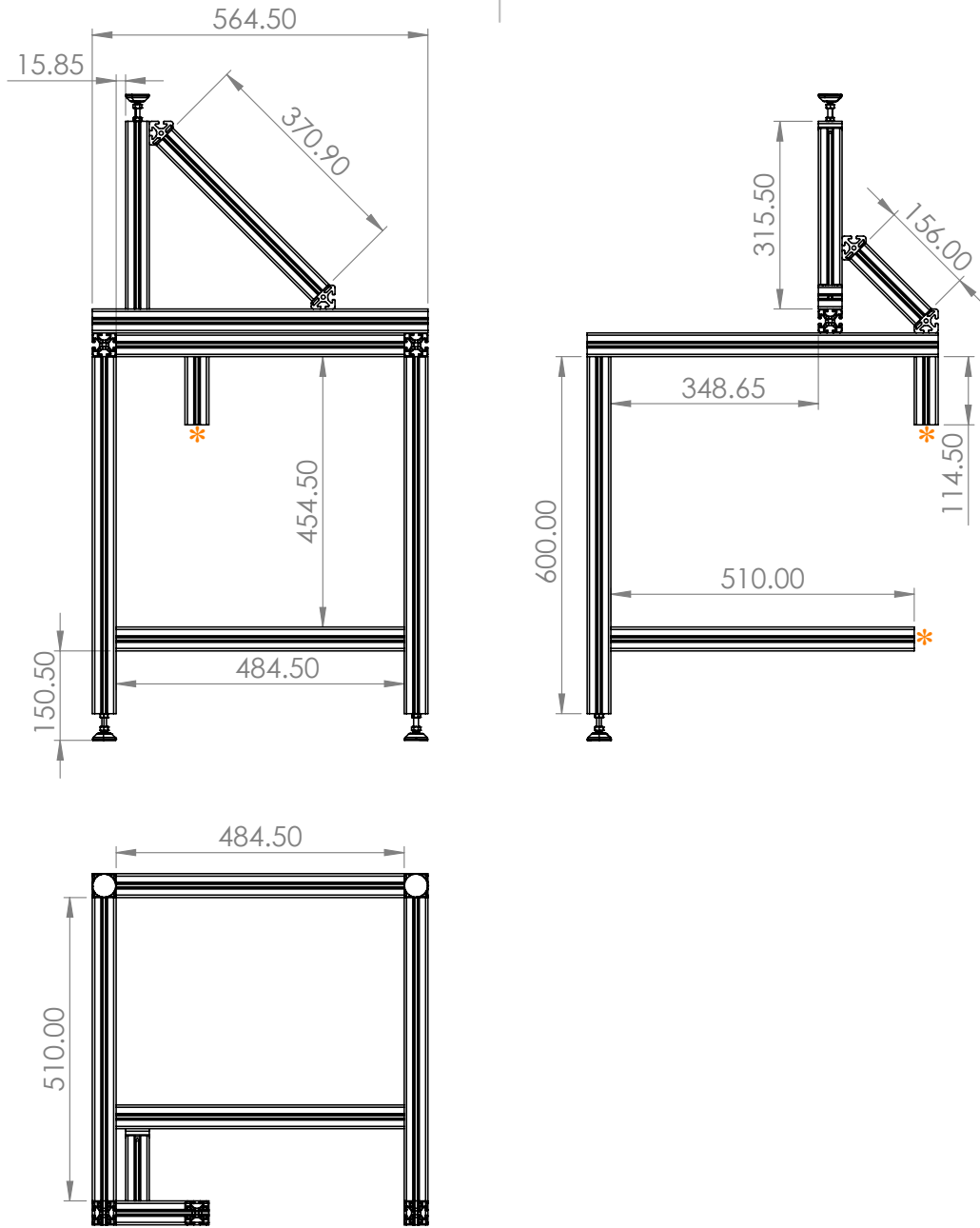


**Figure 49:** SolidWorks drawing of the first EA10+ supporting structure option. An upside-down steel item foot is used to support the analyzer. Apart from the possibility to change the height of the foot by a few centimeters, the setup is limited to one degree of freedom. Dimensions are given in mm, and the orange asterisks mark the spots where the structure is mounted to the NIELS experiment.

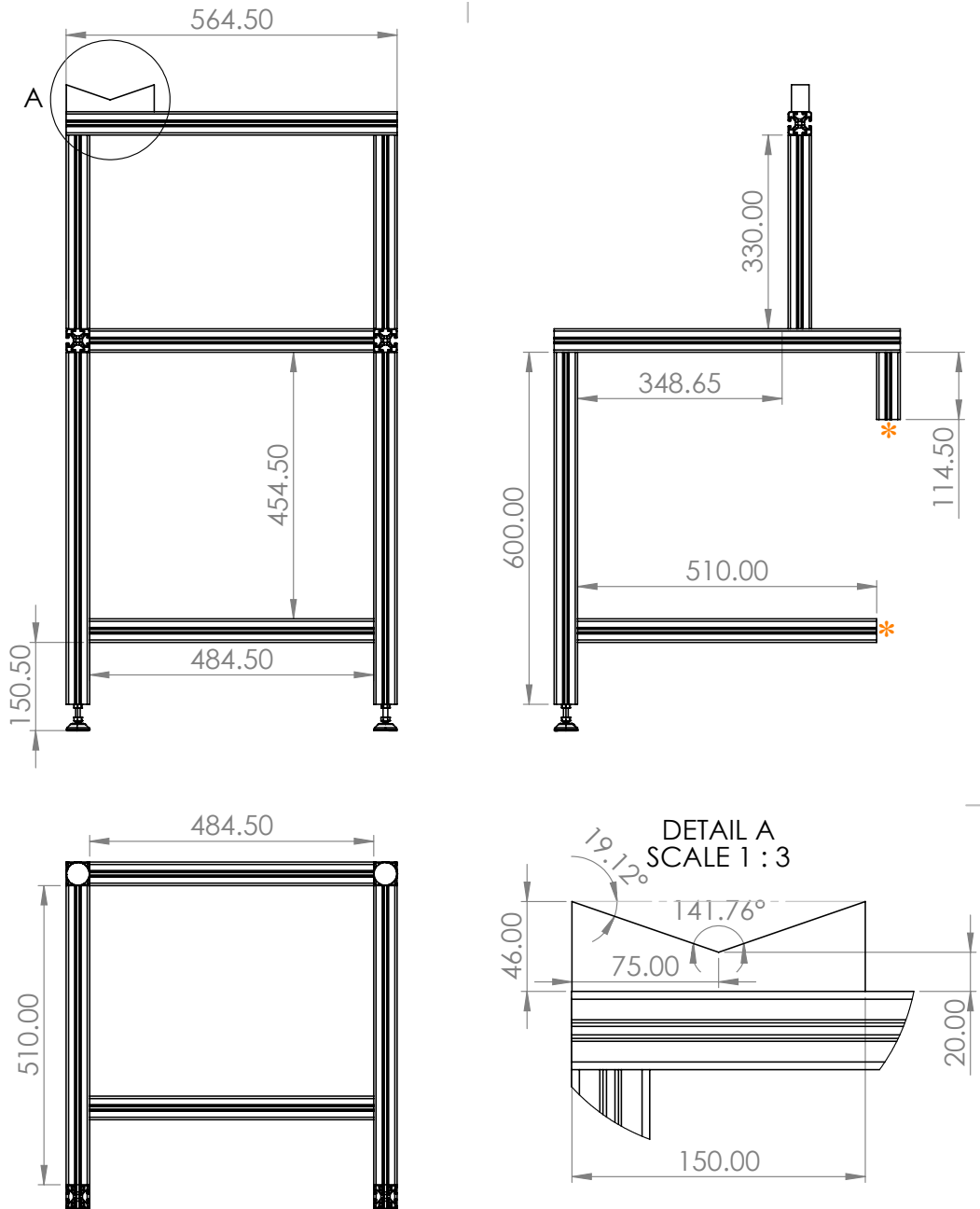


**Figure 50:** SolidWorks drawing of the second and ultimately used EA10+ supporting structure. Its advantages are the improved stability as well as the two horizontal degrees of freedom. Dimensions are given in mm, and the orange asterisk marks the spot where the structure is mounted to the NIELS experiment.

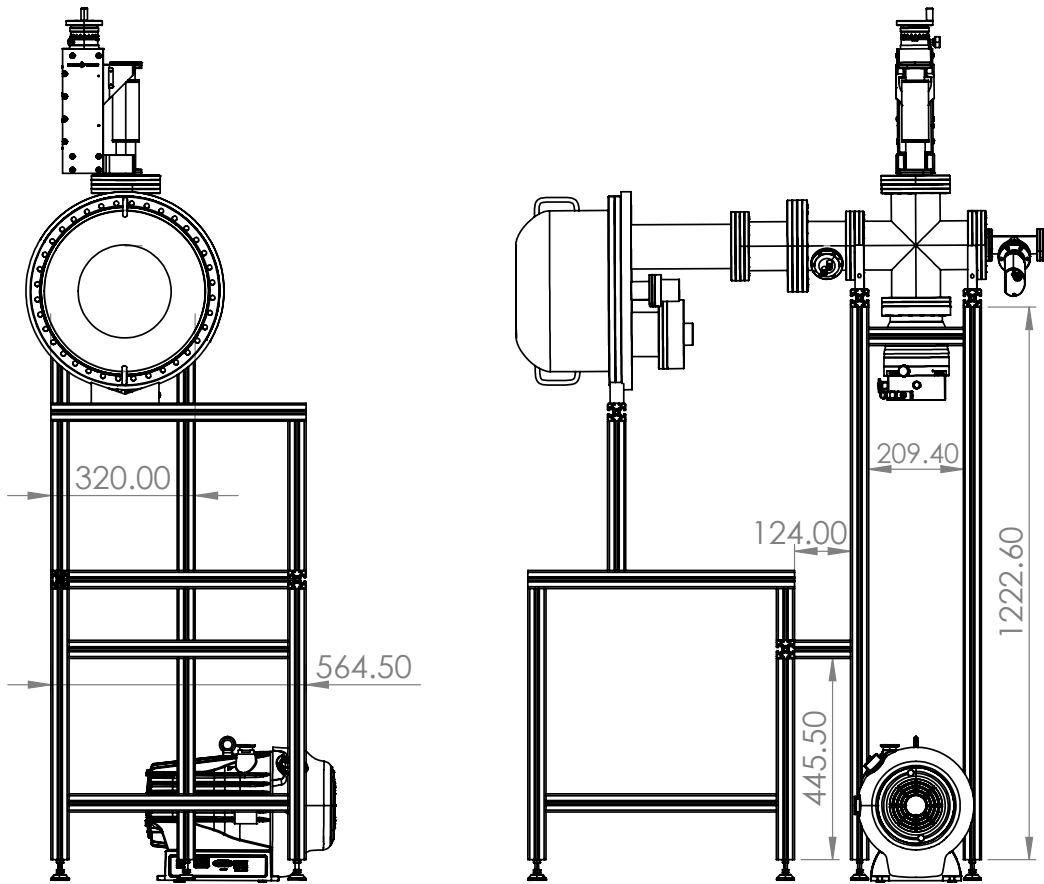


**Figure 51:** SolidWorks drawing of the rig for testing and calibrating the EA10+. The ultimately used setup is shown, with a tungsten wire as electron source, which was placed directly in front of the analyzer opening. Dimensions are given in mm.

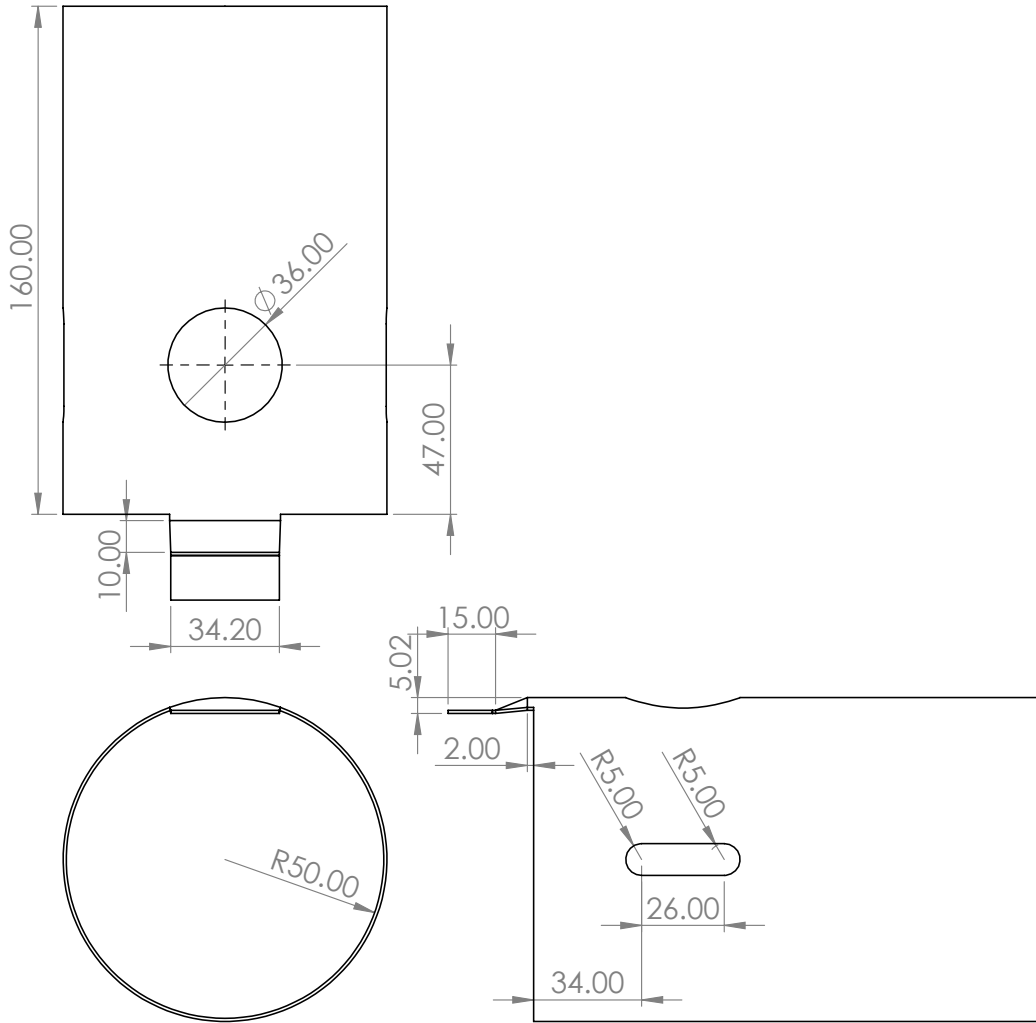


**Figure 52:** SolidWorks drawing of the  $\mu$ -metal shielding used inside the target chamber of NIELS. It was used shield the slow electrons from external magnetic fields. Dimensions are given in mm.

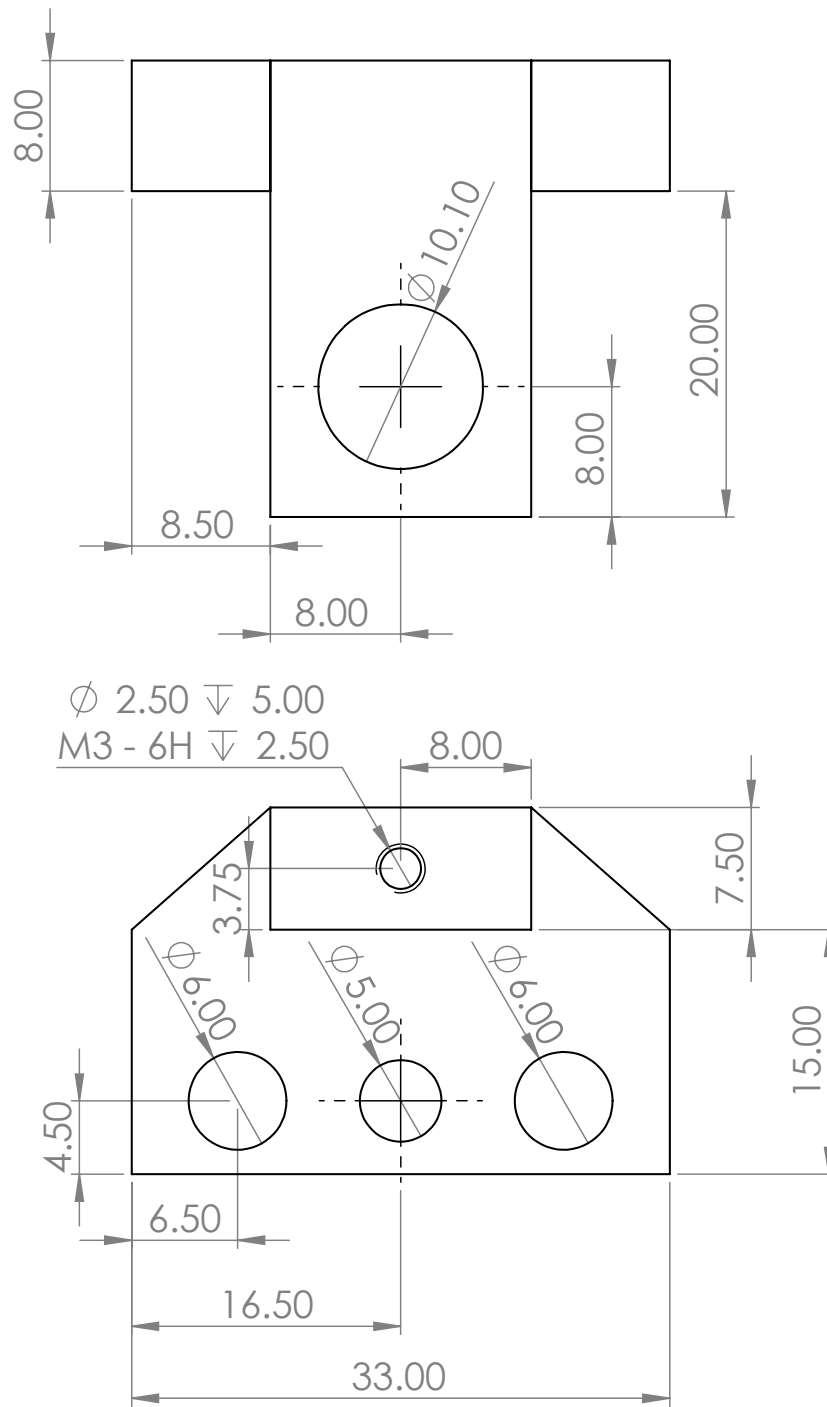


**Figure 53:** SolidWorks drawing of the first part (1/2) of the new target holder, which was used for the measurements. It shows the target plate holder, which is mounted to the manipulator beam. Dimensions are given in mm.

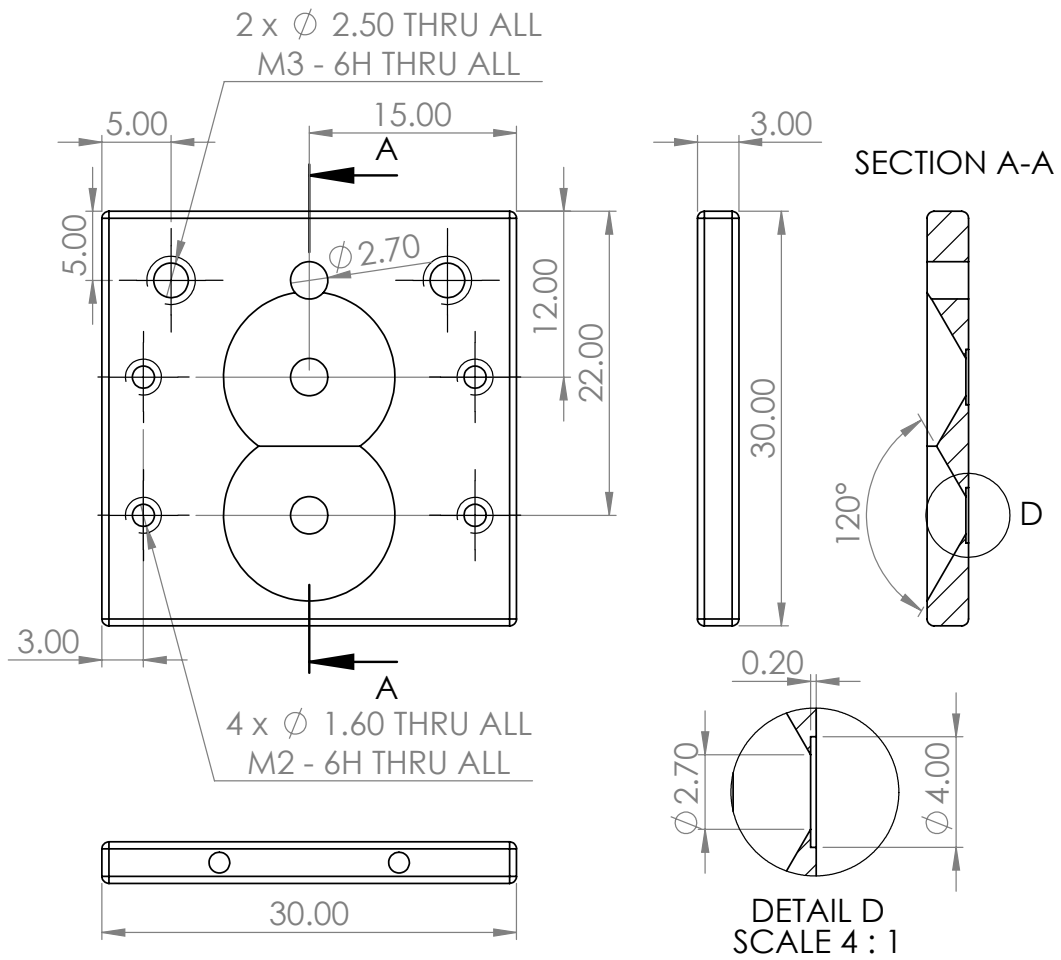


**Figure 54:** SolidWorks drawing of the second part (2/2) of the new target holder, which was used for the measurements. It holds the samples and is mounted to the target plate holder. Dimensions are given in mm.